

Lithium Niobate Piezo-optomechanical Crystals

WENTAO JIANG¹, RISHI N. PATEL¹, FELIX M. MAYOR¹, TIMOTHY P. MCKENNA¹,
 PATRICIO ARRANGOIZ-ARRIOLA¹, CHRISTOPHER J. SARABALIS¹, JEREMY D.
 WITMER¹, RAPHAËL VAN LAER¹, AND AMIR H. SAFAVI-NAEINI¹

¹Department of Applied Physics and Ginzton Laboratory, Stanford University, 348 Via Pueblo Mall, Stanford, California 94305, USA

Compiled March 5, 2019

Demonstrating a device that efficiently connects light, motion, and microwaves is an outstanding challenge in classical and quantum photonics. We make significant progress in this direction by demonstrating a photonic crystal resonator on thin-film lithium niobate (LN) that simultaneously supports high- Q optical and mechanical modes, and where the mechanical modes are coupled piezoelectrically to microwaves. For optomechanical coupling, we leverage the photoelastic effect in LN by optimizing the device parameters to realize coupling rates $g_0/2\pi \approx 120$ kHz. An optomechanical cooperativity $C > 1$ is achieved leading to phonon lasing. Electrodes on the nanoresonator piezoelectrically drive mechanical waves on the beam that are then read out optically allowing direct observation of the phononic bandgap. Quantum coupling efficiency of $\eta \approx 10^{-8}$ from the input microwave port to the localized mechanical resonance is measured. Improvements of the microwave circuit and electrode geometry can increase this efficiency and bring integrated ultra-low-power modulators and quantum microwave-to-optical converters closer to reality.

1. INTRODUCTION

Optomechanical crystals (OMC) provide a powerful platform for engineering interactions between photons and phonons. Colocalizing optical and mechanical modes allows light to control and readout mechanical motion, leading to a large variety of quantum optomechanical experiments [1–5] and enabling routing and transduction of classical and quantum signals between microwave-frequency phonons and optical photons [6–10]. Silicon optomechanical crystals have strong coupling rates but lack intrinsic piezoelectricity [11]. Capacitive and electrostrictive forces in thin-film silicon have been used to drive mechanical resonances [12–14], but a viable way of efficiently coupling to the high-frequency wavelength-scale mechanical modes of an optomechanical crystal resonator is yet to be demonstrated. Thus approaches to coupling OMCs to microwave photons and superconducting qubits have focused on piezoelectric materials such as aluminum nitride (AlN) [15–18], gallium arsenide (GaAs) [19–22] and gallium phosphide (GaP) [23, 24]. However, no platform to date has succeeded in simultaneously demonstrating high optical and mechanical quality factors, large optomechanical coupling, and good piezoelectric coupling efficiency. Recent work on nanopatterned lithium niobate (LN) has addressed sev-

eral of these weaknesses, by showing that high mechanical Q and efficient piezoelectric transduction of localized modes are possible [25, 26], while excellent optical Q 's have been demonstrated in photonic crystals [27, 28] and microring structures [29]. In this work we demonstrate an LN device with sufficiently large optical and mechanical Q s and optomechanical coupling to realize efficient optical transduction of microwave frequency phonons. Considering that efficient microwave transduction has already been realized in the same material system with phononic crystal devices [25], our result solves a key remaining technical challenge required for an LN quantum microwave-to-optical transducer.

Here we demonstrate one-dimensional (1D) nanobeam OMCs on lithium niobate (LN) with optical quality factors above 300,000 at a wavelength of $\lambda \approx 1550$ nm, and a mechanical mode frequency close to 2 GHz possessing quality factors as high as 17,000 at 4 kelvin. The high frequency mechanical mode and narrow optical linewidth allows our system to operate in the resolved-sideband regime, where the mechanical frequency greatly exceeds the cavity decay rate. An important parameter of the system is the zero-point coupling rate g_0 which characterizes the optical frequency jitter induced by the zero-point motion of

the cavity. We make calibrated measurements of optomechanical backaction in addition to measurements of electromagnetically induced transparency (EIT) and absorption (EIA) with different optical pump powers and detunings to extract a zero-point coupling rate of $g_0/2\pi \approx 120$ kHz. The wide bandgap (~ 3.7 eV) of LN allows us to pump $n_{\text{pump}} \sim 1.5 \times 10^5$ intracavity photons without significant degradation of the optical linewidth. This enables us to realize sufficiently large cooperativity $C \propto n_{\text{pump}}$ to observe mechanical lasing under the action of a blue-detuned optical pump. Phonon lasing is an important signature of optomechanical cooperativity $C > 1$, which occurs when the optomechanical backaction exceeds the intrinsic mechanical dissipation in the system, a requirement for realizing efficient phonon-photon conversion [30–34]. Our system performs favorably when compared to other piezo-optomechanical approaches. In particular, OMCs on GaAs show $g_0/2\pi$ on the order of 1 MHz [20], but have not operated in the sideband-resolved regime due to low optical $Q \sim 40,000$. Moreover, $g_0/2\pi \sim 100$ kHz has been achieved on AlN [18], but our LN device possesses somewhat higher optical and mechanical quality factors. Finally we note that all three platforms, AlN [35], GaAs [36], and LN [25, 37] have demonstrated compatibility with superconducting qubit technology and form promising platforms for quantum transduction.

The piezoelectric property of LN enables us to electrically drive the localized mechanical mode with an oscillating microwave electric field using fabricated on-chip electrodes. The electrically generated phonons are detected optomechanically allowing us to measure the piezo-optomechanical response of the OMC. More generally, electrical driving allows us to probe the full mechanical spectrum of the device with far greater sensitivity than is achieved by measuring thermal Brownian motion, as it allows us to drive the modes to a larger amplitude than is possible thermally. This leads to a remarkably clear signature of the mechanical bandgap of the nanobeam mirror unit cell that is visible from the piezo-optomechanical response. Furthermore, we analyze the piezo-optomechanical coupling by calibrating the coherent phonon number from the electrical drive against the known thermal phonon occupancy to infer the effective microwave-mechanics coupling rate $g_\mu/2\pi \sim 2$ kHz that characterizes the rate at which microwave frequency phonons would interact with a microwave frequency resonator (assuming a 50 Ω resonator impedance). Comparing to the mechanical losses, this coupling is about two orders of magnitude away from achieving sufficiently large cooperativity to enable coherent microwave-to-optical conversion.

We have demonstrated that the LN on silicon platform can be engineered to support strong optomechanical coupling between telecom photons and GHz phonons. This further demonstrates that lithium niobate is a material system with enormous potential for quantum electro-optic and optomechanical transduction [17, 21, 25, 38–41]. In addition to piezo-optomechanical transduction, the electro-optic and nonlinear optical properties of LN enable active integrated optical elements and enhanced optical parametric processes [29, 39, 40, 42, 43].

2. DESIGN

We begin with the design and simulation of the 1D OMC on LN. Due to imperfections in the LN nanofabrication process, the resulting inside and outside sidewall angles are approximately $\theta_{\text{in}} = 22^\circ$ and $\theta_{\text{out}} = 11^\circ$ from the vertical direction. As a result, the nanobeam no longer possesses the reflection symmetry about

the xy -plane, which we call z -symmetry. Given a structure that has y -symmetry, as long as the material properties also remain invariant under reflection about the xz -plane, the modes can be classified according to their y -symmetry. For optical waves, material properties will be invariant as long as the Z is in the longitudinal direction of the beam. For mechanical waves in LN, the situation is a bit more complicated due to the anisotropic elastic properties that generally break the y -symmetry, even for a symmetric structure with the Z -axis aligned along the nanobeam. In the special case where the nanobeam is fabricated on Y -cut LN and is parallel to the crystal Z axis, one of the crystal mirror planes coincides with the y -symmetry plane of the nanobeam geometry, and the y -symmetry is restored. Under this configuration, the optical and mechanical modes can be classified according to their y -symmetry properties.

We adapt the design recipe demonstrated for silicon OMCs [11] to LN considering our etch properties and material anisotropy. We first design a mirror unit cell with quasi-TE optical bandgap of 30 THz at X -point around 194 THz and a partial mechanical bandgap from 1.48 GHz to 2.17 GHz for y -symmetric mechanical modes. The geometry of the mirror cell is shown in fig. 1(a), with outer width $w_1 = 1247$ nm, inner width $w_2 = 919$ nm, $h_x = 330$ nm, $h_y = 859$ nm, thickness $t = 300$ nm and lattice constant $a = 558$ nm. We use a sinusoid-shaped outer edge to realize a larger air-hole. Fig. 1(c) and fig. 1(d) show the optical and mechanical band structures of the mirror cell. The corresponding bandgaps are emphasized as pink shaded regions.

To localize optical and mechanical modes, we focus on the X -point fundamental quasi-TE optical mode and the Γ -point mechanical breathing mode. By reducing the lattice constant and the separation between the air-holes, the X -point optical mode shifts up in frequency and the Γ -point breathing mode frequency is reduced, putting both modes inside their corresponding bandgaps. Using multivariable genetic optimization, defect cell geometry parameters are found to be $(a, w_2, h_x, h_y) = (450, 1092, 334, 811)$ nm by maximizing $g_0 \min(Q, Q_{\text{th}})/Q_{\text{th}}$, where g_0 is the optomechanical coupling rate, Q is the radiation-limited optical quality factor and $Q_{\text{th}} = 10^7$ is chosen to ignore unachievably high Q [11]. The full nanobeam is generated by a smooth transition from the mirror cell geometry to the defect cell geometry. The variation of the parameters is shown in fig. 1(f) together with the finite-element method simulated [44] fundamental TE optical mode (fig. 1(g)) and mechanical breathing mode (fig. 1(h)). The LN thickness t and the outer edge w_1 are kept the same for the full nanobeam. The global and material coordinate systems are shown at the bottom-left of fig. 1(h). The in-plane rotation angle ϕ is defined as the angle between crystal axis Z and global axis x for both X -cut and Y -cut LN (supplementary material). The dashed (dotted) arrow represents crystal $Y(X)$ axis for $X(Y)$ -cut LN. We obtained a radiation-limited optical quality factor $Q \sim 4 \times 10^6$ and an effective mode volume as small as $\sim 0.2(\lambda/n)^3$ for the simulated fundamental optical mode at $\omega_c/2\pi = 200$ THz. The simulated mechanical breathing mode is at $\omega_m/2\pi = 2.1$ GHz with effective mass $m_{\text{eff}} = 645$ fg and zero-point motion $x_{\text{zp}} = 2.48$ fm. The mode profiles are modified slightly by the crystal orientation. The primary effect of the orientation however is the variation in the optomechanical coupling due to anisotropic nature of the photoelastic effect – this is studied in more detail in the supplementary material.

The lack of y -symmetry in general induces leakage of phonons into other propagating modes (blue bands in Fig. 1d) of the beam by making nominally disallowed transitions pos-

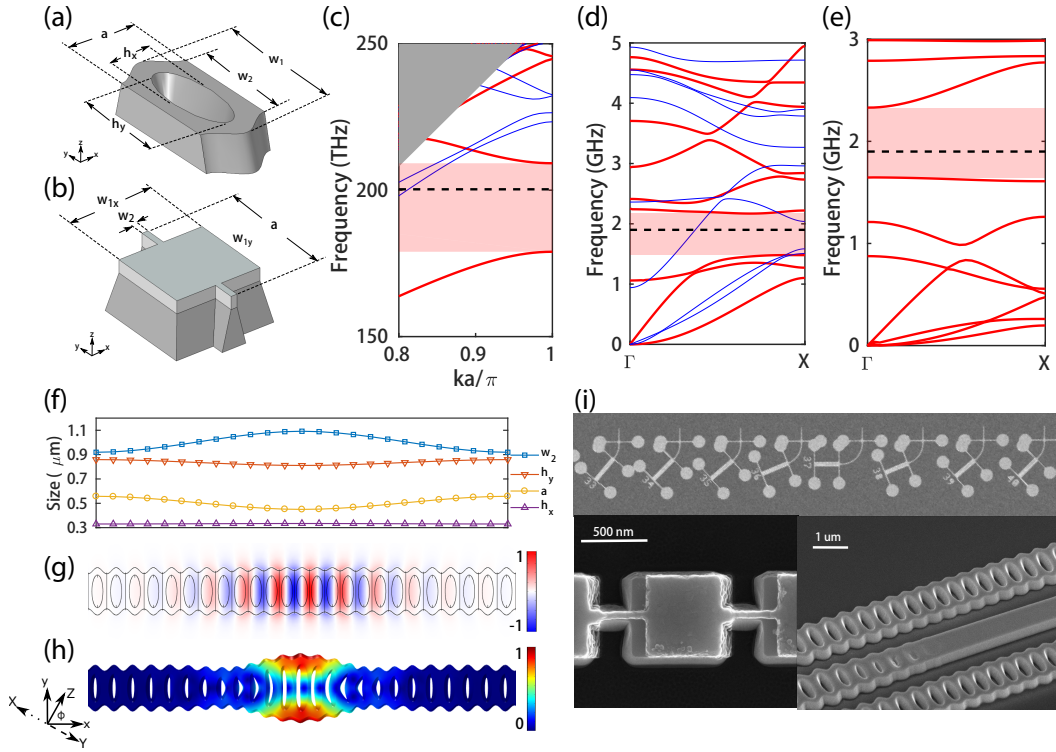


Fig. 1. One-dimensional optomechanical crystal (OMC) design. (a) Unit cell geometry of the nanobeam OMC, showing definitions of the parameters. (b) Unit cell geometry of the 1D phononic shield. The direction of the periodicity is perpendicular to the direction of the nanobeam. The (c) optical and (d) mechanical band structure of the nanobeam unit cell. The bands are classified by y -symmetry (red) and y -antisymmetry (blue). In (c), the gray shaded region represents the continuum of radiation modes. The pink shaded regions highlight the bandgap for quasi-TE optical modes (c) and symmetric mechanical modes (d). The dashed black lines correspond to the localized fundamental TE optical mode and the mechanical breathing mode of the nanobeam respectively. (e) Mechanical band structure of the 1D phononic shield unit cell, showing a complete bandgap around 2 GHz. (f) Variations of unit cell parameters along the nanobeam. w_1 is kept constant for all unit cells. (g) E_y component of the optical mode. (h) Displacement field of the breathing mode. The global and material coordinates are shown (see text for description). (i) Scanning electron micrograph (SEM) of the fabricated device. Top: one row of devices with different nanobeam orientations, taken before the aluminum lift-off step. Bottom left: top view of the 1D phononic shield region, showing both the LN pattern and the Al electrodes. Misalignment on the order of 20 nm is visible. Bottom right: SEM of two nanobeams coupled to one reflector.

sible as has been studied in previous work on silicon structures [45]. To reduce the effect of this source of mechanical dissipation, we implement a 1D phononic shield (PS) to anchor the nanobeam [11, 46]. The geometry of the PS unit cell is shown in fig. 1(b), including the top aluminum electrode layer with thickness $t_m = 100$ nm. The dimensions of this PS unit cell are chosen to be $(a, w_{1x}, w_{1y}, w_2) = (1000, 600, 650, 50)$ nm such that the mechanical band structure of the unit cell opens up a full bandgap from 1.65 GHz to 2.33 GHz (fig. 1(e)). The effect of the metallization layer has been taken into account in these simulations.

3. FABRICATION

In contrast to silicon, nanofabrication of LN is known to suffer from a lack of an effective chemical etch. However, since the development and commercial availability of thin-film LN on silicon oxide [47, 48], high- Q micro-ring resonators and photonic crystals have been demonstrated with physical argon milling and reactive ion etching [27, 28, 49–52]. We adopt an argon milling process similar to Ref. [49] for patterning the OMC structure.

The OMCs are fabricated on a lithium niobate on silicon

(LNOS) wafer, with an initial LN thickness of $t \approx 500$ nm. The LN layer is first thinned to $t = 300$ nm with argon ion milling. The nanobeam geometry is defined by electron beam lithography (EBL) with HSQ resist. The pattern is then transferred to the LN layer by argon ion milling. The remaining HSQ is removed with 2 minute 5:1 buffered oxide etch (BOE). A second aligned EBL with CSAR resist followed by a liftoff process defines the aluminum metal layer. The device is finally released with a masked XeF_2 dry etch that selectively removes the silicon. Electrical contacts between on-chip electrodes and aluminum wires are made with ultrasonic wire-bonding. Tapered optical mode converters are patterned on the LN layer with efficiency $\eta \sim 50\%$ for coupling the OMCs to a lensed fiber [9].

Fig. 1(i) shows scanning electron micrographs of the resulting structures taken before the release step. A notable feature of the sample is that it contains many devices with the identical OMC design, but where we have rotated the orientation of the nanobeam with respect to the crystal axis (see also Ref. [20] for similar measurements on GaAs). This is done to give us a better understanding of the anisotropic photoelastic property of LN and its effect on the performance of the OMCs.

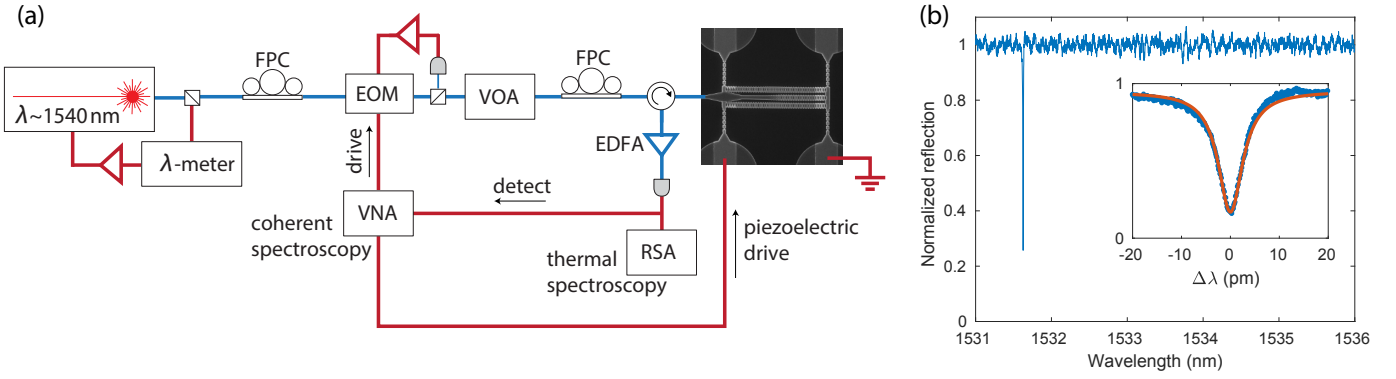


Fig. 2. Measurement setup and optical mode characterization. (a) Simplified diagram of the measurement setup. Two LN optomechanical crystals are side-coupled to a reflector. The reflection spectrum is recorded for optical characterization. The thermal mechanical motion of the nanobeam encoded in the optical noise power spectrum is measured by the realtime spectrum analyzer (RSA). A weak optical sideband is generated with the vector network analyzer (VNA) and electro-optic modulator (EOM) for coherent spectroscopy. The mechanical motion can be also piezoelectrically driven and the transduced optical sidebands are measured by the high-speed photodetector and the VNA. (b) Optical reflection spectrum of an LN OMC. A zoomed-in wavelength sweep shows a loaded optical quality factor $Q = 2.5 \times 10^5$ and corresponding intrinsic quality factor $Q_i = 3.5 \times 10^5$ (inset, blue: data, red: fit). Variable optical attenuator (VOA), erbium-doped fiber amplifier (EDFA), fiber polarization controller (FPC).

4. OPTOMECHANICAL CHARACTERIZATION AND MECHANICAL LASING

We measured the devices at both room temperature and at low temperature, by cooling to 4 K inside a closed-cycle Montana Instruments cryostat. The actual temperature of the phonon mode in the cryostat is closer to ~ 20 K. This is determined by calibrated thermal spectroscopy as explained in Ref. [9]. The measurement setup, shown in fig. 2(a), is suited for understanding the optical and mechanical properties of the system. The optical properties were first characterized by scanning a continuous-wave tunable laser and monitoring the reflection spectrum. Fig. 2(b) shows a typical optical reflection spectrum with one sharp resonance from the localized optical mode. A narrow scan near the resonance is fit to a Lorentzian lineshape to determine the linewidth and quality factor (fig. 2(b) inset). For the device under consideration, a loaded Q of 2.5×10^5 and an intrinsic Q of 3.5×10^5 are extracted, corresponding to a total linewidth $\kappa/2\pi = 776$ MHz that is significantly smaller than the mechanical frequency and puts us in the resolved sideband regime of cavity optomechanics [31]. Similar measurements taken over multiple devices, as detailed in the supplementary materials, show no apparent correlation between the optical quality factors and the crystal orientations.

A well known effect in optical resonators is the shift in their frequency proportional to intracavity photon number n_c . This nonlinearity can result from the thermo-optic, or Kerr effect. In our measurements, we observe a strikingly different relation between intracavity photon number and cavity resonance shift. As n_c is increased, we see that the cavity frequency shifts by a frequency proportional to n_c^2 . The shift becomes easily measurable at roughly $n_c \gtrsim 10^4$, when it exceeds the linewidth. At these values and larger, it is observed to be quadratic. In addition to measuring the frequency shift, we use a sideband probe to measure the cavity linewidth at different optical powers and detunings (see SI for full dataset). Based on the amount of linewidth broadening that is observed ($\sim 15\%$ at $n_c = 1.5 \times 10^5$), we attribute the quadratic thermal shift to absorption of the intracavity photons, where this absorption rate itself has a linear

dependence on n_c . This dependence distinguishes it from green-induced infrared absorption (GRIIRA) [53], in which case the absorption rate of intracavity photons would scale as n_c^2 (the second harmonic intensity) instead of the observed n_c . Moreover, it is likely not due to absorption of second-harmonic generated photons, which would produce the correct n_c^2 thermal shift, but would also require a significant reduction in the cavity linewidth to explain the observed thermal shift. A detailed understanding of the physical mechanism behind this heating and the development of methods for its mitigation (such as surface treatment [22] or Mg-doping [53]) will be the subject of future investigations.

The optomechanical coupling between the localized optical mode and mechanical mode gives rise to an interaction Hamiltonian $\hat{H}_{\text{int}} = \hbar g_0 \hat{a}^\dagger \hat{a} (\hat{b} + \hat{b}^\dagger)$, where g_0 is the zero-point optomechanical coupling rate, \hat{a} and \hat{b} are the annihilation operator for the optical and mechanical modes respectively. When the optical mode is driven by a laser beam up to an intracavity photon number $n_c \gg 1$, the interaction can be linearized to $\hat{H}_{\text{int}} = \hbar G (\hat{a} + \hat{a}^\dagger) (\hat{b} + \hat{b}^\dagger)$, and $G = g_0 \sqrt{n_c}$ is the effective optomechanical coupling rate [31]. The optomechanical (OM) backaction leads to a frequency shift and an extra damping rate of the mechanical mode given by [31]

$$\gamma_{\text{OM}} = G^2 \left(\frac{\kappa}{\kappa^2/4 + (\Delta - \omega_m)^2} - \frac{\kappa}{\kappa^2/4 + (\Delta + \omega_m)^2} \right), \quad (1)$$

where κ is the total optical mode linewidth, $\Delta = \omega_c - \omega_l$ is the cavity-laser detuning and ω_m is the mechanical mode frequency. In the sideband-resolved regime where $\omega_m > \kappa$, only the first term is appreciable for a red detuned pump laser with $\Delta \sim \omega_m$, while for blue side pumping, the second term dominates. As shown in fig. 2(a), the mechanical properties of the system can be characterized by either measuring the transduced mechanical thermal motion in the optical noise power spectral density (thermal spectroscopy), or by measuring the effect of the mechanical response on a weak optical probe generated by the electro-optic modulator (coherent spectroscopy).

The optomechanical coupling rates are observed to peak at $\phi = 135^\circ$ on X-cut LN. This is in agreement with simulations outlined in detail in the supplementary materials. We focus

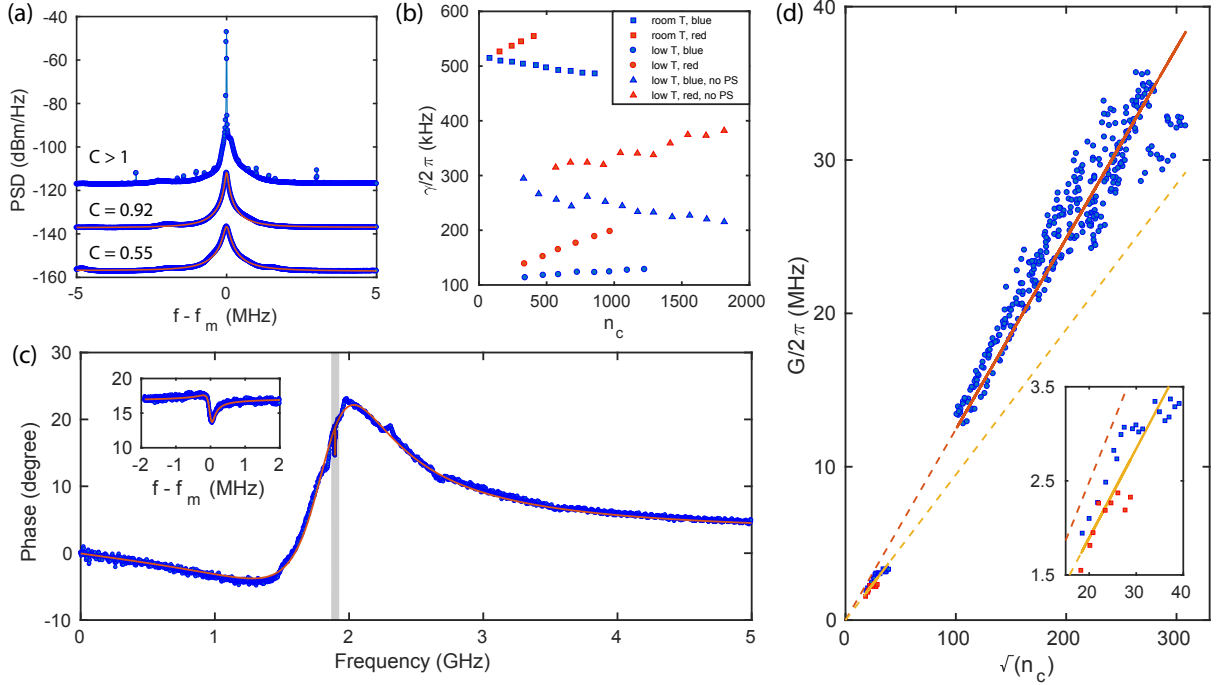


Fig. 3. EIT and optomechanical backaction measurements. (a) Power spectral density of the mechanical motion induced optical sideband. Measured spectrum with same optical power and different detunings are shown with corresponding cooperativities, vertically displaced for viewing purposes. When a pump laser beam is blue detuned near $\Delta \approx -\omega_m$, mechanical lasing results as the cooperativity exceeds unity. The spectrum without mechanical lasing is fitted (red) for the total mechanical linewidth γ_{tot} . (b) Total mechanical linewidth versus intracavity photon numbers under different conditions (blue: $\Delta = -\omega_m$, red: $\Delta = \omega_m$). For the low temperature results, one OMC without the 1D phononic shield are measured for comparison (\triangle). (c) Measured phase response of the optical probe beam at low power pump with detuning $\Delta = \omega_m$ at low temperature (blue dots) and fit (red line). Inset: zoom-in data and fit near the transparency window. (d) Effective optomechanical coupling rate G extracted from the EIT responses at low temperature versus the square root of intracavity photon numbers $\sqrt{n_c}$. High-power optical pump at detunings $-\omega_m < \Delta < 0$ is adopted to achieve high n_c without introducing mechanical lasing. Linear fits for high n_c (orange) and low n_c (yellow) measurements are both shown for comparison. Inset: detail of the low n_c region, with data from both blue (blue) and red (red) detuned pump.

on one device with this specific orientation and characterize its mechanical and optomechanical properties. We first perform the thermal spectroscopy at low temperature with a blue detuned laser pump, where the OM backaction is simplified to

$$\gamma_{\text{OM}} = -\frac{G^2\kappa}{\kappa^2/4 + (\Delta + \omega_m)^2}. \quad (2)$$

We fix the pump power $P_{\text{in}} \sim 0.2$ mW and step the detuning towards $\Delta = -\omega_m$ to increase the optomechanical cooperativity $C \equiv |\gamma_{\text{OM}}/\gamma_i|$, where γ_i is the intrinsic mechanical linewidth. Fig. 3(a) shows three different power spectral densities of the reflected pump laser at different values of cooperativity. When $C > 1$ is reached, the total mechanical linewidth $\gamma_{\text{tot}} = \gamma_i + \gamma_{\text{OM}}$ becomes negative. The system enters an oscillating regime and a mechanical lasing peak emerges in the power spectrum.

To extract the intrinsic mechanical linewidth γ_i and zero-point optomechanical coupling rate g_0 of the same device, we fit γ_{tot} from the power spectrum. We fix cavity-laser detuning $\Delta = \pm\omega_m$ so the OM backaction is given by $\gamma_{\text{OM}} = \pm 4G^2/\kappa = \pm 4g_0^2 n_c/\kappa$, resulting in a linear relationship between γ_{OM} and n_c . We adopted small pump powers $P_{\text{in}} \sim 10$ μ W in order to access stable red-detuned measurements in the presence of a

thermal cavity red shift. As shown in fig. 3(b), we measured the device at both room and low temperature and on the blue and red sides. The intrinsic mechanical loss γ_i is reduced by a factor of 5 after cooling the device. We observe that γ_{tot} deviates from simple predictions only considering OM backaction, showing an asymmetry with respect to the intrinsic linewidth between blue and red detuned laser pump frequency. The deviation becomes larger when the device is cooled down, where no linewidth reduction is observed with a blue detuned pump laser. We attribute the deviation to thermally-induced linewidth broadening which scales linearly with respect to n_c for low pump powers and is independent of the sign of the detuning. At higher pump powers, the thermally-induced broadening saturates near $\gamma_{\text{tot}}/\pi \approx 300$ kHz and as a result, the OM backaction eventually dominates the linewidth change, leading to mechanical lasing. We combine the measurements from $\Delta = \pm\omega_m$ at low powers to eliminate the thermal broadening. We measure $g_0/2\pi = 128$ kHz, intrinsic mechanical linewidth $\gamma_i/2\pi = 513$ kHz at room temperature and $g_0/2\pi = 92$ kHz, $\gamma_i/2\pi = 109$ kHz at low temperature. The cause of the temperature dependence of g_0 may be attributed to a temperature dependence of the photoelastic coefficients, but is not well under-

tood at this time. The corresponding mechanical quality factor is $Q_m \sim 3500$ at room temperature and $Q_m \sim 17000$ at low temperature. A device with identical design but without a 1D phononic shield is also measured at low temperature for comparison (Δ), showing $g_0/2\pi = 108$ kHz and $\gamma_i/2\pi = 284$ kHz.

The optomechanical properties of the same device are also measured at low temperature using the optical sideband probe measurement (coherent spectroscopy). A typical frequency-dependent phase response of the probe is plotted in fig. 3(c). The response from the optical cavity is apparent in this measurement. Additionally, we observe electromagnetically induced transparency, visible in the phase variation near the mechanical frequency [54–57]. The data shown was measured with optical pump detuning $\Delta = \omega_m$. The corresponding cooperativity C determines the size of the EIT feature. By fitting the phase response of the probe, we obtain an independent measurement of the optical mode linewidth κ , the intrinsic mechanical mode frequency ω_m and linewidth γ_i , and also the effective optomechanical coupling strength G [55].

We extracted G with different intracavity photon number n_c in fig. 3(d). Measurements with n_c approaching 10^5 were achieved by using high pump powers at detunings $-\omega_m < \Delta < 0$ to avoid mechanical lasing. The relation between G and $\sqrt{n_c}$ is determined by fitting the low-power and high-power measurements independently. The results of these fits are shown in fig. 3(d) as yellow and orange lines, extended for comparison. From these fits, we extracted zero point couplings of $g_0/2\pi = 127 \pm 9$ kHz for high n_c and $g_0/2\pi = 96 \pm 10$ kHz for low n_c . We find reasonable agreement of g_0 between back-action measurement at low (high) temperature and EIT/EIA measurement at low (high) n_c . An important figure of merit is g_0/κ which for this system is 10^{-4} , making it comparable to competing implementations in AlN, SiN_x and GaAs [32].

5. PIEZO-OPTOMECHANICAL CHARACTERIZATION

We have fully characterized the optomechanical system by thermal and coherent spectroscopy. Beyond the conventional optomechanical measurements, the piezoelectricity of LN allows us to directly drive the mechanical motion of the OMC, revealing more details of the mechanical spectrum. To access piezoelectricity, we pattern aluminum electrodes on the LN layer that can be driven with an oscillating voltage. The separation between the edges of the electrodes are chosen to be $d_{\text{metal}} = 22$ μm such that there's no degradation on the optical quality factor. When a voltage is applied on the aluminum electrodes in the nanobeam mirror cell region, an electric field parallel to the nanobeam is generated and deforms the optomechanical crystal. The deformation can be sensitively read out by the laser utilizing the optomechanical coupling.

The piezoelectric coupling between the OMC mechanical mode and the microwave channel (with impedance $Z_0 = 50$ Ω) is modeled as an external coupling induced decay rate γ_e . Our goal is to determine γ_e by an optomechanically calibrated measurement of the piezomechanical driving efficiency. We pump the optical mode at $\Delta \sim \omega_m$ and drive the mechanics through the microwave channel. The coherent amplitude of the mechanical motion from standard input-output theory is (supplementary material)

$$\beta = \frac{-\sqrt{\gamma_e} c_{\text{in}}}{i(\omega_m - \omega_\mu) + \gamma_{\text{tot}}/2}, \quad (3)$$

where c_{in} is the input microwave field ($|c_{\text{in}}|^2$ is the microwave photon flux), $\omega_\mu \sim \omega_m$ is the microwave signal frequency and

$\gamma_{\text{tot}} = \gamma_i + \gamma_e + \gamma_{\text{OM}}$ is the total mechanical linewidth. The transduced optical field amplitude is

$$\alpha = \frac{-iG\beta}{i(\Delta - \omega_\mu) + \kappa/2}. \quad (4)$$

We readout the beat tone between α and the pump laser, giving us the piezo-optomechanical $S_{21}(\omega)$.

Fig. 4(a) shows the piezo-optomechanical S_{21} taken on a Y-cut LN nanobeam with in-plane rotation $\phi = 0$ at room temperature. We have chosen this orientation and ϕ so that the electrodes only drive the symmetric mechanical bands. The oscillating electric field not only modulates the optical mode frequency via the driven mechanical motion, but also through the electro-optic effect of LN. We repeat the same $S_{21}(\omega)$ measurement with different cavity-laser detuning Δ . The optical cavity response filters the electro-optically generated sidebands, leading to a broad feature with linewidth κ in the coherent response. A series of sharper peaks are also visible, and arise from the piezoelectric driving of mechanical resonances of the OMC structure. We also observe a ‘‘clean’’ frequency range which matches reasonably well with the simulated mechanical bandgap of the nanobeam mirror cell (shaded region in fig. 4(a)). The localized mechanical modes can be identified near the upper edge of the bandgap. The disordered response outside the bandgap region is not due to noise of the instrument or measurement device, and is observed consistently with the same spectrum. This is likely due to complicated mixing of modes outside of the bandgap.

The mechanical origin of the narrow piezo-optomechanical response peaks can be verified by comparing with the thermal spectroscopy results. Fig. 4(b) shows the piezo-optomechanical response near the upper bandgap edge, including three Fano-shaped peaks. The thermal mechanical noise power spectrum of the same frequency range is shown in fig. 4(c). Fano-shaped response peaks in the piezo-optomechanical S_{21} match closely with the thermal-mechanical noise peaks in the power spectral density. We further calibrate the coherent phonon number from the electrical drive with the thermal phonon occupancy (supplementary material). The decay rate $\gamma_e/2\pi = 8.8 \pm 0.56$ mHz is obtained between the microwave transmission line and the localized mechanical mode. The resulting external microwave-to-mechanics conversion efficiency is $\eta_{\text{ext}} = \gamma_e/\gamma \sim 10^{-8}$. We attribute this low efficiency to the large separation between the coupling electrodes and the impedance mismatch between the electrodes and the $Z_0 = 50$ Ω transmission line.

If the OMC were to be connected to a microwave resonator with the same coupling electrode configuration, the microwave-mechanics coupling rate would be $g_\mu = \sqrt{\gamma_e \omega_m} \cdot \sqrt{Z_c/Z_0}/2$, where Z_c is the characteristic impedance of the microwave resonator (supplementary material). Based on the measurement of γ_e and assuming $Z_c = 50$ Ω , we estimate $g_\mu/2\pi \sim 2$ kHz. Microwave resonators with impedance on the order of $Z_c \sim 5$ k Ω can be fabricated with high-kinetic-inductance superconducting nanowires [58] and spiral inductors [59]. By optimizing the configuration of the coupling electrodes and engineering the mechanical mode leakage [41, 45], strong coupling between the microwave resonator and mechanical mode of the OMC can be realized if $\gamma_e/2\pi \gtrsim 1$ Hz and $Z_c/Z_0 \sim 100$, giving $g_\mu/2\pi \gtrsim 100$ kHz $\gtrsim \gamma/2\pi$.

6. CONCLUSIONS

In summary, we have demonstrated high quality optomechanical crystals on a lithium-niobate-on-silicon platform in the

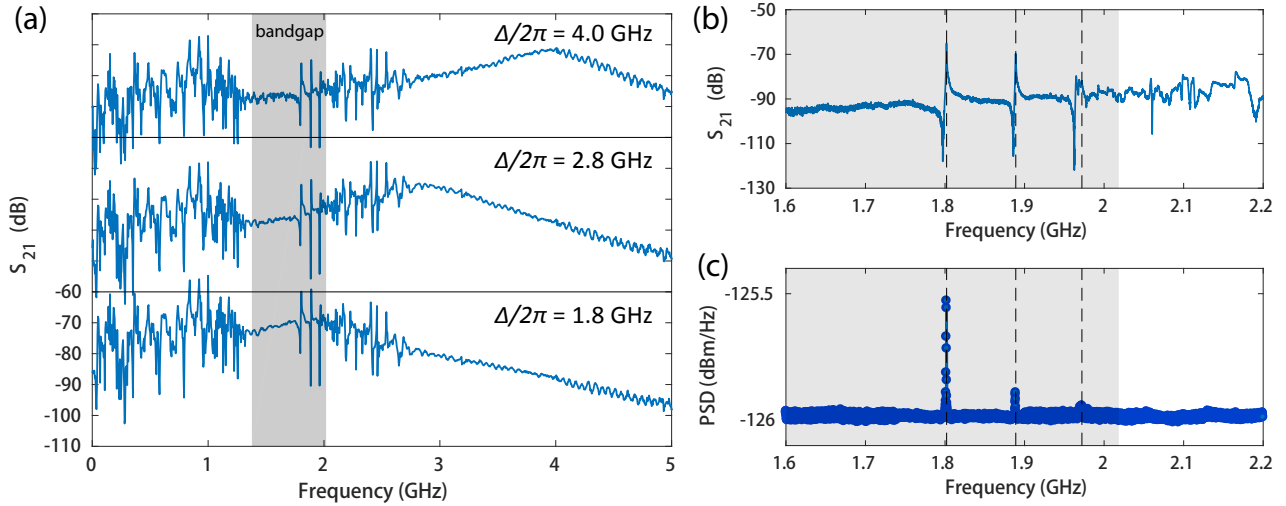


Fig. 4. Piezo-optomechanical measurements. (a) Optical readout of electro-optically and piezoelectrically driven optical sideband for different pump detunings. Broad electro-optic effect induced peak shifts when changing pump detuning, while mechanical responses stay at the same frequency. The gray shaded area corresponds to the simulated mechanical bandgap of the nanobeam mirror unit cell. The mechanical response outside the bandgap is disordered but repeatable. (b) Piezo-optomechanical response near the upper bandgap edge. Peaks of the response match well with the thermal mechanical peaks from the power spectral density (c), corresponding to the localized mechanical breathing modes of the nanobeam.

resolved-sideband regime. We measure optical quality factors above 300,000 and mechanical quality factors as high as 17,000 at cryogenic temperature. We measure optomechanical back-action, electromagnetic induced transparency and absorption to extract $g_0/2\pi \sim 120$ kHz. We observed minor degradation ($\lesssim 15\%$) of the optical linewidth with intracavity photon number n_c up to 1.5×10^5 . Mechanical lasing is observed with blue-detuned laser pump, corresponding to a cooperativity above unity. Red-detuned measurements with relatively high n_c is not feasible due to the observed quadratic thermal-optic shift, which may be reduced by doping LN with MgO [53]. Given the strong nonlinear optic effect and electro-optic effect of LN, our high quality LN OMC provides a promising platform for nonlinear photonic application and densely integrated active on-chip photonic and phononic elements.

We further utilize the piezoelectricity of LN to drive the OMC. The mechanical bandgap and localized mechanical modes of the OMC are identified. Based on the measured microwave-to-mechanical conversion rate, we estimate the coupling rate between the OMC and a microwave resonator with identical coupling configuration to be $g_\mu/2\pi \sim 2$ kHz. The microwave-mechanics coupling strength can be improved by reducing the coupling electrodes separation and increasing the characteristic impedance of the microwave resonator. With the recent advance of strong coupling between nanomechanical structures on LN and superconducting circuits [25, 37], a full microwave-to-optical conversion is within reach with our LN OMC platform, opening up opportunities for both classical and quantum signal storing, processing and transduction in hybrid systems exploiting densely integrated electrical, mechanical and optical elements [32].

FUNDING INFORMATION

National Science Foundation (NSF) (1708734, 1808100, 1542152), Army Research Office (ARO/LPS) (CQTS), Office of Naval Re-

search (ONR) (MURI No. N00014-151-2761), Fonds Wetenschappelijk Onderzoek (FWO Marie Skłodowska-Curie grant agreement No. 665501), VOCATIO.

ACKNOWLEDGMENT

P.A.A. and J.D.W. are partly supported by the Stanford University SGF program. R.N.P. is partly supported by the NSF Graduate Research Fellowships Program. A.S.N. and W.J. thank Martin Fejer and Marek Pechal for numerous helpful discussions. We thank Thaibao Phan supplying us with HSQ. Device fabrication was performed at the Stanford Nano Shared Facilities (SNSF) and the Stanford Nanofabrication Facility (SNF).

REFERENCES

1. J. Chan, T. M. Alegre, A. H. Safavi-Naeini, J. T. Hill, A. Krause, S. Gröblacher, M. Aspelmeyer, and O. Painter, "Laser cooling of a nanomechanical oscillator into its quantum ground state," *Nature* **478**, 89 (2011).
2. A. H. Safavi-Naeini, J. Chan, J. T. Hill, T. P. M. Alegre, A. Krause, and O. Painter, "Observation of quantum motion of a nanomechanical resonator," *Phys. Rev. Lett.* **108**, 033602 (2012).
3. J. T. Hill, A. H. Safavi-Naeini, J. Chan, and O. Painter, "Coherent optical wavelength conversion via cavity optomechanics," *Nat. Commun.* **3**, 1196 (2012).
4. J. D. Cohen, S. M. Meenehan, G. S. MacCabe, S. Gröblacher, A. H. Safavi-Naeini, F. Marsili, M. D. Shaw, and O. Painter, "Phonon counting and intensity interferometry of a nanomechanical resonator," *Nature* **520**, 522 (2015).
5. I. Marinković, A. Wallucks, R. Riedinger, S. Hong, M. Aspelmeyer, and S. Gröblacher, "Optomechanical bell test," *Phys. Rev. Lett.* **121**, 220404 (2018).
6. K. Stannigel, P. Rabl, A. S. Sørensen, P. Zoller, and M. D. Lukin, "Optomechanical transducers for long-distance

- quantum communication," *Phys. Rev. Lett.* **105**, 220501 (2010).
7. K. Fang, M. H. Matheny, X. Luan, and O. Painter, "Optical transduction and routing of microwave phonons in cavity-optomechanical circuits," *Nat. Photonics* **10**, 489 (2016).
 8. K. Fang, J. Luo, A. Metelmann, M. H. Matheny, F. Marquardt, A. A. Clerk, and O. Painter, "Generalized non-reciprocity in an optomechanical circuit via synthetic magnetism and reservoir engineering," *Nat. Phys.* **13**, 465 (2017).
 9. R. N. Patel, Z. Wang, W. Jiang, C. J. Sarabalis, J. T. Hill, and A. H. Safavi-Naeini, "Single-mode phononic wire," *Phys. Rev. Lett.* **121**, 040501 (2018).
 10. R. Riedinger, A. Wallucks, I. Marinković, C. Löschner, M. Aspelmeyer, S. Hong, and S. Gröblacher, "Remote quantum entanglement between two micromechanical oscillators," *Nature* **556**, 473 (2018).
 11. J. Chan, A. H. Safavi-Naeini, J. T. Hill, S. Meenehan, and O. Painter, "Optimized optomechanical crystal cavity with acoustic radiation shield," *Appl. Phys. Lett.* **101**, 081115 (2012).
 12. D. Weinstein and S. A. Bhawe, "The Resonant Body Transistor," *Nano Lett.* **10**, 1234–1237 (2010).
 13. R. Van Laer, R. N. Patel, T. P. McKenna, J. D. Witmer, and A. H. Safavi-Naeini, "Electrical driving of X-band mechanical waves in a silicon photonic circuit," *APL Photonics* **3**, 086102 (2018).
 14. M. Kalaei, M. Mirhosseini, P. B. Dieterle, M. Peruzzo, J. M. Fink, and O. Painter, "Quantum electromechanics of a hypersonic crystal," *Nat. Nanotechnol.* (2019).
 15. W. Pernice, C. Xiong, C. Schuck, and H. Tang, "High-q aluminum nitride photonic crystal nanobeam cavities," *Appl. Phys. Lett.* **100**, 091105 (2012).
 16. L. Fan, X. Sun, C. Xiong, C. Schuck, and H. X. Tang, "Aluminum nitride piezo-acousto-photonic crystal nanocavity with high quality factors," *Appl. Phys. Lett.* **102**, 153507 (2013).
 17. J. Bochmann, A. Vainsencher, D. D. Awschalom, and A. N. Cleland, "Nanomechanical coupling between microwave and optical photons," *Nat. Phys.* **9**, 712 (2013).
 18. A. Vainsencher, K. Satzinger, G. Peairs, and A. Cleland, "Bi-directional conversion between microwave and optical frequencies in a piezoelectric optomechanical device," *Appl. Phys. Lett.* **109**, 033107 (2016).
 19. L. Ding, C. Baker, P. Senellart, A. Lemaitre, S. Ducci, G. Leo, and I. Favero, "Wavelength-sized gaas optomechanical resonators with gigahertz frequency," *Appl. Phys. Lett.* **98**, 113108 (2011).
 20. K. C. Balram, M. Davanço, J. Y. Lim, J. D. Song, and K. Srinivasan, "Moving boundary and photoelastic coupling in gaas optomechanical resonators," *Optica* **1**, 414–420 (2014).
 21. K. C. Balram, M. I. Davanço, J. D. Song, and K. Srinivasan, "Coherent coupling between radiofrequency, optical and acoustic waves in piezo-optomechanical circuits," *Nat. photonics* **10**, 346 (2016).
 22. M. Forsch, R. Stockill, A. Wallucks, I. Marinkovic, C. Gärtner, R. A. Norte, F. van Otten, A. Fiore, K. Srinivasan, and S. Gröblacher, "Microwave-to-optics conversion using a mechanical oscillator in its quantum groundstate," *arXiv preprint arXiv:1812.07588* (2018).
 23. M. Mitchell, A. C. Hryciw, and P. E. Barclay, "Cavity optomechanics in gallium phosphide microdisks," *Appl. Phys. Lett.* **104**, 141104 (2014).
 24. K. Schneider, P. Welter, Y. Baumgartner, S. Hönl, H. Hahn, L. Czornomaz, and P. Seidler, "Optomechanics with one-dimensional gallium phosphide photonic crystal cavities," in *Quantum Nanophotonics*, vol. 10359 (International Society for Optics and Photonics, 2017), p. 103590K.
 25. P. Arrangoiz-Arriola, E. A. Wollack, M. Pechal, J. D. Witmer, J. T. Hill, and A. H. Safavi-Naeini, "Coupling a superconducting quantum circuit to a phononic crystal defect cavity," *Phys. Rev. X* **8**, 031007 (2018).
 26. L. Shao, S. Maity, L. Wu, A. Shams-Ansari, Y.-I. Sohn, E. Puma, M. Gadalla, M. Zhang, C. Wang, and M. Lončar, "High-q gigahertz surface acoustic wave cavity on lithium niobate," *arXiv preprint arXiv:1901.09080* (2019).
 27. H. Liang, R. Luo, Y. He, H. Jiang, and Q. Lin, "High-quality Lithium Niobate Photonic Crystal Nanocavities," *Optica* **4**, 1251 (2017).
 28. M. Li, H. Liang, R. Luo, Y. He, and Q. Lin, "High-q two-dimensional lithium niobate photonic crystal slab nanoresonators," *arXiv preprint arXiv:1806.04755* (2018).
 29. C. Wang, C. Langrock, A. Marandi, M. Jankowski, M. Zhang, B. Desiatov, M. M. Fejer, and M. Lončar, "Ultrahigh-efficiency wavelength conversion in nanophotonic periodically poled lithium niobate waveguides," *Optica* **5**, 1438–1441 (2018).
 30. A. H. Safavi-Naeini and O. Painter, "Proposal for an optomechanical traveling wave phonon–photon translator," *New J. Phys.* **13**, 013017 (2011).
 31. M. Aspelmeyer, T. J. Kippenberg, and F. Marquardt, "Cavity optomechanics," *Revs. Mod. Phys.* **86**, 1391–1452 (2014).
 32. A. H. Safavi-Naeini, D. Van Thourhout, R. Baets, and R. Van Laer, "Controlling phonons and photons at the wavelength scale: integrated photonics meets integrated phononics," *Optica* **6**, 213 (2019).
 33. T. Kippenberg, H. Rokhsari, T. Carmon, A. Scherer, and K. Vahala, "Analysis of radiation-pressure induced mechanical oscillation of an optical microcavity," *Phys. Rev. Lett.* **95**, 033901 (2005).
 34. W. C. Jiang and Q. Lin, "Chip-scale cavity optomechanics in lithium niobate," *Sci. Reports* **6**, 36920 (2016).
 35. A. D. O'Connell, M. Hofheinz, M. Ansmann, R. C. Bialczak, M. Lenander, E. Lucero, M. Neeley, D. Sank, H. Wang, M. Weides *et al.*, "Quantum ground state and single-phonon control of a mechanical resonator," *Nature* **464**, 697 (2010).
 36. L. R. Sletten, B. A. Moores, J. J. Viennot, and K. W. Lehnert, "Resolving phonon fock states in a multimode cavity with a double-slit qubit," *arXiv preprint arXiv:1902.06344* (2019).
 37. P. Arrangoiz-Arriola, E. A. Wollack, Z. Wang, M. Pechal, W. Jiang, T. P. McKenna, J. D. Witmer, and A. H. Safavi-Naeini, "Resolving the energy levels of a nanomechanical oscillator," *arXiv preprint arXiv:1902.04681* (2019).
 38. J. D. Witmer, J. A. Valery, P. Arrangoiz-Arriola, C. J. Sarabalis, J. T. Hill, and A. H. Safavi-Naeini, "High-q photonic resonators and electro-optic coupling using silicon-lithium-niobate," *Sci. Reports* **7**, 46313 (2017).
 39. C. Wang, M. Zhang, B. Stern, M. Lipson, and M. Lončar, "Nanophotonic lithium niobate electro-optic modulators," *Opt. Express* **26**, 1547–1555 (2018).
 40. C. Wang, M. Zhang, X. Chen, M. Bertrand, A. Shams-Ansari, S. Chandrasekhar, P. Winzer, and M. Lončar, "Integrated lithium niobate electro-optic modulators operating at cmos-compatible voltages," *Nature* **562**, 101 (2018).
 41. P. Arrangoiz-Arriola and A. H. Safavi-Naeini, "Engineering

- interactions between superconducting qubits and phononic nanostructures,” *Phys. Rev. A* **94**, 063864 (2016).
42. C. Wang, X. Xiong, N. Andrade, V. Venkataraman, X.-F. Ren, G.-C. Guo, and M. Lončar, “Second harmonic generation in nano-structured thin-film lithium niobate waveguides,” *Opt. Express* **25**, 6963–6973 (2017).
 43. H. Jiang, H. Liang, R. Luo, X. Chen, Y. Chen, and Q. Lin, “Nonlinear frequency conversion in one dimensional lithium niobate photonic crystal nanocavities,” *Appl. Phys. Lett.* **113**, 021104 (2018).
 44. “Comsol multiphysics 5.0,” <https://www.comsol.com>.
 45. R. N. Patel, C. J. Sarabalis, W. Jiang, J. T. Hill, and A. H. Safavi-Naeini, “Engineering phonon leakage in nanomechanical resonators,” *Phys. Rev. Appl.* **8**, 041001 (2017).
 46. A. H. Safavi-Naeini and O. Painter, “Design of optomechanical cavities and waveguides on a simultaneous bandgap phononic-photonic crystal slab,” *Opt. Express* **18**, 14926–14943 (2010).
 47. H. Hu, R. Ricken, and W. Sohler, “Lithium niobate photonic wires,” *Opt. express* **17**, 24261–24268 (2009).
 48. G. Poberaj, H. Hu, W. Sohler, and P. Guenter, “Lithium niobate on insulator (Lnoi) for micro-photonic devices,” *Laser & photonics reviews* **6**, 488–503 (2012).
 49. C. Wang, M. J. Burek, Z. Lin, H. A. Atikian, V. Venkataraman, I.-C. Huang, P. Stark, and M. Lončar, “Integrated high quality factor lithium niobate microdisk resonators,” *Opt. express* **22**, 30924–30933 (2014).
 50. H. Hartung, E.-B. Kley, A. Tünnermann, T. Gischkat, F. Schrempel, and W. Wesch, “Fabrication of ridge waveguides in zinc-substituted lithium niobate by means of ion-beam enhanced etching,” *Opt. letters* **33**, 2320–2322 (2008).
 51. M. Zhang, C. Wang, R. Cheng, A. Shams-Ansari, and M. Lončar, “Monolithic ultra-high-q lithium niobate microring resonator,” *Optica* **4**, 1536–1537 (2017).
 52. I. Krasnokutska, J.-L. J. Tambasco, X. Li, and A. Peruzzo, “Ultra-low loss photonic circuits in lithium niobate on insulator,” *Opt. express* **26**, 897–904 (2018).
 53. Y. Furukawa, K. Kitamura, A. Alexandrovski, R. Route, M. Fejer, and G. Foulon, “Green-induced infrared absorption in mgo doped linbo 3,” *Appl. Phys. Lett.* **78**, 1970–1972 (2001).
 54. S. Weis, R. Rivière, S. Deléglise, E. Gavartin, O. Arcizet, A. Schliesser, and T. J. Kippenberg, “Optomechanically induced transparency,” *Science*. **330**, 1520–1523 (2010).
 55. A. H. Safavi-Naeini, T. M. Alegre, J. Chan, M. Eichenfield, M. Winger, Q. Lin, J. T. Hill, D. E. Chang, and O. Painter, “Electromagnetically induced transparency and slow light with optomechanics,” *Nature*. **472**, 69 (2011).
 56. F. Massel, S. U. Cho, J.-M. Pirkkalainen, P. J. Hakonen, T. T. Heikkilä, and M. A. Sillanpää, “Multimode circuit optomechanics near the quantum limit,” *Nat. Commun.* **3**, 987 (2012).
 57. A. H. Safavi-Naeini, J. T. Hill, S. Meenehan, J. Chan, S. Gröblacher, and O. Painter, “Two-dimensional phononic-photonic band gap optomechanical crystal cavity,” *Phys. Rev. Lett.* **112**, 153603 (2014).
 58. N. Samkharadze, A. Bruno, P. Scarlino, G. Zheng, D. DiVincenzo, L. DiCarlo, and L. Vandersypen, “High-kinetic-inductance superconducting nanowire resonators for circuit qed in a magnetic field,” *Phys. Rev. Appl.* **5**, 044004 (2016).
 59. S. Barzanjeh, M. Wulf, M. Peruzzo, M. Kalaei, P. Dieterle, O. Painter, and J. Fink, “Mechanical on-chip microwave circulator,” *Nat. Commun.* **8**, 953 (2017).
 60. A. Andrushchak, B. Mytsyk, H. Laba, O. Yurkevych, I. Solskii, A. Kityk, and B. Sahraoui, “Complete sets of elastic constants and photoelastic coefficients of pure and mgo-doped lithium niobate crystals at room temperature,” *J. Appl. Phys.* **106**, 073510 (2009).
 61. T. Carmon, L. Yang, and K. J. Vahala, “Dynamical thermal behavior and thermal self-stability of microcavities,” *Opt. Express* **12**, 4742–4750 (2004).
 62. X. Sun, H. Liang, R. Luo, W. C. Jiang, X.-C. Zhang, and Q. Lin, “Nonlinear optical oscillation dynamics in high-q lithium niobate microresonators,” *Opt. Express* **25**, 13504–13516 (2017).
 63. D. I. Schuster, *Circuit quantum electrodynamics* (Yale University, 2007).
 64. S. J. Bosman, M. F. Gely, V. Singh, D. Bothner, A. Castellanos-Gomez, and G. A. Steele, “Approaching ultrastrong coupling in transmon circuit qed using a high-impedance resonator,” *Phys. Rev. B* **95**, 224515 (2017).
 65. J. Chan, “Laser cooling of an optomechanical crystal resonator to its quantum ground state of motion,” Ph.D. thesis, California Institute of Technology (2012).
 66. R. Weis and T. Gaylord, “Lithium niobate: Summary of physical properties and crystal structure,” *Appl. Phys. A* **37**, 191–203 (1985).
 67. “Mathematica,” Available from <http://www.wolfram.com>.

Supplementary Information

A. ORIENTATION DEPENDENCY OF OMC PROPERTIES

A. Definition of coordinate systems and rotated dielectric and photoelastic tensor

We start by defining the coordinate systems. The global coordinate system is fixed with the nanobeam with axis labeled by x, y, z , and the material coordinate system coincides with the crystal axis of LN, denoted by X, Y, Z . Note that for Euler angles which rotate the axis of the global coordinate system to the material coordinate system, the corresponding rotation matrix can be applied to transform the tensor components in the material system to the global system.

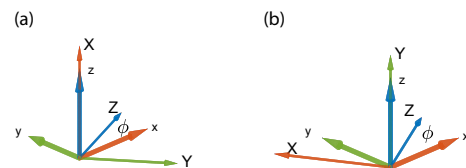


Fig. 5. Definition of the coordinate systems for (a) X-cut LN and (b) Y-cut LN. The global coordinate system is shown with thicker and shorter arrows, labeled with x, y, z . The material coordinate systems are shown with thinner and longer arrows, labeled with X, Y, Z . The nanobeam is parallel to the global x axis. The in-plane rotation angle ϕ is defined as the angle between x and Z axis in both case.

We first give the rotation matrix used for X-cut LN (LNX) and Y-cut LN (LNY) with in-plane rotation angle ϕ as

$$R_{\text{LNX}}(\phi) = \begin{bmatrix} 0 & \sin \phi & \cos \phi \\ 0 & -\cos \phi & \sin \phi \\ 1 & 0 & 0 \end{bmatrix}, \quad (5)$$

$$R_{\text{LNY}}(\phi) = \begin{bmatrix} -\sin \phi & 0 & \cos \phi \\ \cos \phi & 0 & \sin \phi \\ 0 & 1 & 0 \end{bmatrix}. \quad (6)$$

The global coordinate system and the rotated material systems are shown in fig. 5. The corresponding Euler angles in 'z-x-z' convention are $(\alpha, \beta, \gamma) = (\phi - \pi/2, -\pi/2, -\pi/2)$ for LNX and $(\alpha, \beta, \gamma) = (\phi - \pi/2, -\pi/2, \pi)$ for LNY.

The photoelastic tensor components of the rotated crystal in the global coordinate system are then given by

$$p'_{ijkl}(\phi) = R_{im}(\phi)R_{jn}(\phi)R_{kp}(\phi)R_{lq}(\phi)p_{mnpq}. \quad (7)$$

Repeated indices are to be summed. The components of the rotated photoelastic tensor in the global coordinate system are given in Sec. F.

For both LNX and LNY, the rotated dielectric tensor is

$$\epsilon' = \begin{bmatrix} \epsilon_{11} + \Delta\epsilon_{eo} \cos^2 \phi & \cos \phi \sin \phi \Delta\epsilon_{eo} & 0 \\ \cos \phi \sin \phi \Delta\epsilon_{eo} & \epsilon_{11} + \Delta\epsilon_{eo} \sin^2 \phi & 0 \\ 0 & 0 & \epsilon_{11} \end{bmatrix}, \quad (8)$$

where $\Delta\epsilon_{eo} = \epsilon_{33} - \epsilon_{11}$.

B. Simulation of optomechanical coupling rate

With the rotated dielectric and photoelastic tensor components, the photoelastic contribution of the optomechanical coupling is given by [11]

$$g_{0,\text{PE}} = -\frac{\omega_c}{2} \frac{\int \mathbf{E} \cdot \frac{\partial \epsilon}{\partial \alpha} \cdot \mathbf{E} dV}{\int \mathbf{E} \cdot \mathbf{D} dV}, \quad (9)$$

where α parametrizes the mechanical motion amplitude, and $\partial \epsilon_{ij} / \partial \alpha = -\epsilon_{ik} \epsilon_{lj} p_{klmn} S_{mn} / \epsilon_0$. For isotropic media with refractive index n , the photoelastic induced change in dielectric constant simplifies to $\partial \epsilon_{ij} / \partial \alpha = -\epsilon_0 n^4 p_{ijmn} S_{mn}$.

Consider the qualitative dependence of photoelastic contribution to the optomechanical coupling rate g_0 . For breathing mechanical modes, the dominating strain component is S_{yy} in the global coordinate system. Similarly, for TE optical modes, the primary electric field component is E_y . As a result, the largest photoelastic contribution to g_0 is from $E_y^2 \partial \epsilon_{yy} / \partial \alpha \approx -\epsilon_0 n^4 p'_{22} S_{yy} E_y^2$. This suggests that we focus on the p'_{22} component of the rotated crystal in the global coordinate system.

We use photoelastic components from Ref. [60] for numerical evaluations. The p'_{22} component of LNX and LNY is plotted in fig. 6. The maximal p'_{22} can be achieved on LNX with $\phi = 135$ degree, where $p'_{22} = (p_{11} + p_{33} + p_{13} + p_{31})/4 + p_{44} - (p_{14} + p_{41})/2 \approx 0.3$.

For the moving boundary contribution of the optomechanical interaction, we approximate LN as an isotropic dielectric material with refractive index $n = \sqrt{\epsilon_{\text{LN}}} = 2.2$. The contribution from moving boundary is [11]

$$g_{0,\text{MB}} = -\frac{\omega_c}{2} \frac{\oint (\mathbf{Q} \cdot \mathbf{n}) (\Delta \epsilon E_{\parallel}^2 - \Delta \epsilon^{-1} \mathbf{D}_{\perp}^2) dS}{\int \mathbf{E} \cdot \mathbf{D} dV}, \quad (10)$$

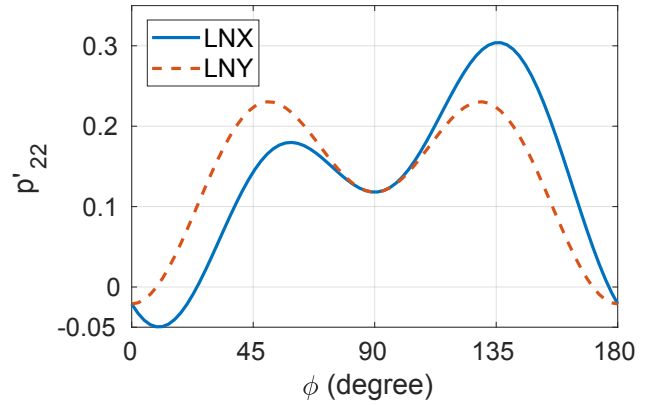


Fig. 6. Rotated photoelastic tensor component p'_{22} for LNX (solid blue) and LNY (dashed red).

where $\Delta \epsilon \equiv \epsilon_{\text{LN}} - \epsilon_{\text{air}}$, $\Delta \epsilon^{-1} \equiv \epsilon_{\text{LN}}^{-1} - \epsilon_{\text{air}}^{-1}$, \mathbf{Q} is the normalized displacement field and \mathbf{n} is the surface norm pointing towards the air. The subscripts \parallel and \perp denote the parallel and perpendicular component of the fields locally with respect to the surface.

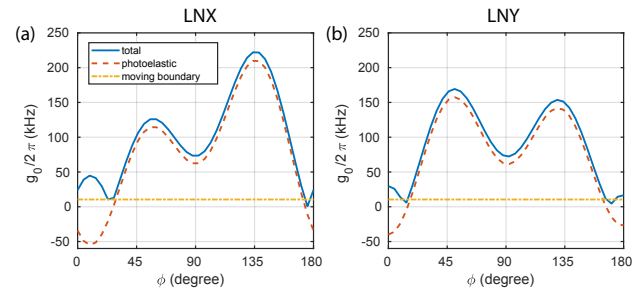


Fig. 7. Simulation of optomechanical coupling rate g_0 on (a) X-cut and (b) Y-cut LN for different in-plane rotation angle ϕ .

We assume same mode profiles for different ϕ as a first-order approximation to calculate the ϕ -dependence of the optomechanical coupling rate g_0 . We evaluate eq. 9 and eq. 10 for different ϕ . In fig. 7 we show the photoelastic contribution $g_{0,\text{PE}}$ (dashed red), moving boundary contribution $g_{0,\text{MB}}$ (dashed dotted yellow) and the absolute values of the total g_0 (blue). From fig. 6, it is clear that p'_{22} is a good indicator of the optomechanical coupling rate.

C. Measurements of optical quality factors and optomechanical coupling rates with various ϕ

We fabricated OMCs on both LNX and LNY with various values of ϕ . The measured optical quality factors are shown in fig. 8(a, b). No obvious dependence of quality factors on ϕ is observed. The quality factors on LNY are generally lower due to fabrication variations between different chips. The mechanical quality factors at room temperature are typically $Q_m \sim 4000$. The room-temperature Q_m is limited by thermoelastic damping and is relatively insensitive to crystal orientations. At cryogenic temperature, the highest mechanical $Q_m = 37,000$ is observed on the LNY OMC with $\phi = 0$, where the y-symmetry of the nanobeam is recovered.

In fig. 8(c, d) we show the measured optomechanical coupling rates g_0 versus OMC orientation angle ϕ . The coupling

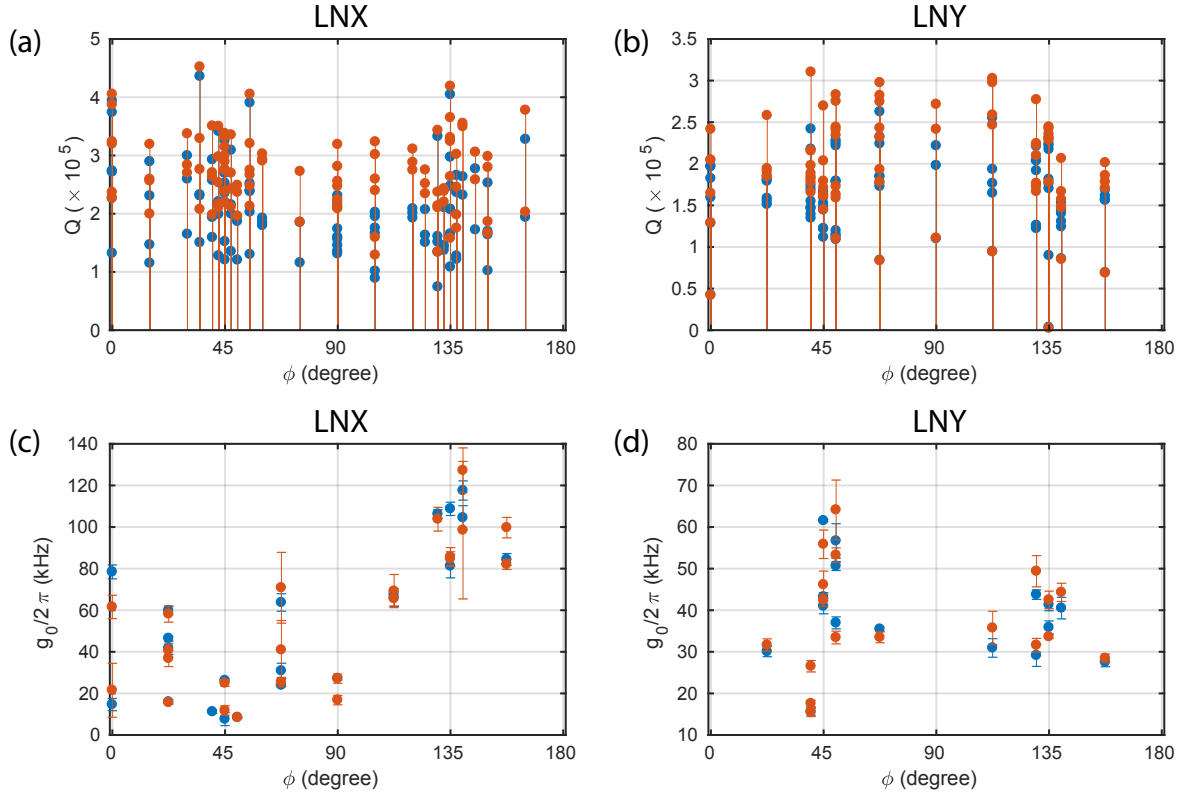


Fig. 8. Optical quality factor Q and optomechanical coupling rate g_0 on LNX and LNY. (a, b) Measured total (blue) and intrinsic (red) optical quality factors on LNX (a) and LNY (b). No obvious dependency on in-plane rotation ϕ can be observed. The quality factors on LNY are generally lower due to fabrication variations between different chips. (c, d) Measured zero-point optomechanical coupling rate g_0 for different ϕ on LNX (c) and LNY (d). Blue (red) data points represent measurement with detuning $\Delta = -\omega_m$ ($\Delta = \omega_m$). Error bars represent one standard deviation obtained by repeated measurements with different laser pump power.

rates were measured at room temperature (300 K) using calibrated thermal mechanical noise power spectral density [9]. The measured g_0 's are in general roughly smaller than the simulated values by $\sim 50\%$. We attribute this discrepancy to the approximation of mode profiles, the fact that the design is only optimized for $\phi = 0$ on LNY, the possible differences in the material properties between simulation and the actual LNOS wafers, and the considerable uncertainties of LN's photoelastic components [60].

Despite the discrepancy between the absolute values of the simulated and measured g_0 , we observe that the maximal optomechanical coupling rate occurs at $\phi = 135^\circ$ on LNX, agreeing with the simulations (fig. 7(a)) and also the simple prediction from p'_{22} (fig. 6). The optimal orientations on LNY are near $\phi = 45^\circ$ and $\phi = 135^\circ$, reasonably matching the simulation results in fig. 7(b).

B. THERMAL-OPTICAL SHIFT AND THERMAL RELAXATION

A. Thermal-optical shift

We observed a thermal-induced optical shift when scanning the laser over the optical cavity with different powers. The thermal-induced optical shift is well understood in silicon microcavities [61]. To better understand the thermal-optical shift on LN OMC, we briefly describe the silicon case here.

In silicon microcavities, the heat absorption rate is proportional to the intracavity photon number n_c , leading to a local temperature change proportional to n_c . The temperature change affects the optical mode via thermal expansion and temperature-dependent refractive index change, both result in a wavelength shift that's linear with respect to the temperature change. A positive wavelength shift is usually observed for an increase in temperature. When the laser frequency approaches the optical cavity from the blue side, n_c , the temperature increase, and the optical cavity shifts red. When the laser reaches beyond the maximum wavelength shift which occurs for maximum n_c at the reflection dip, n_c starts decreasing. The cavity shifts back towards the blue side as a result of decreasing n_c , which further decreases n_c . This causes the cavity to jump back to nearly its original wavelength. The cavity red shift reflects itself in the continuous blue-to-red laser wavelength sweep as a slow slope which gets flatter for higher power. The mode escapes after the laser has passed the maximum shifted wavelength, giving a sharp jump in the transmission or reflection spectrum similar to Fig 9(a).

The thermal-induced optical shift $\Delta\lambda$ we observed on the LN OMC is qualitatively similar to silicon, but the wavelength shifts faster than linear and could be as large as few nanometers at high laser powers. As shown in fig. 9(a), the reflections were measured for linearly increasing laser scan powers, vertically displaced for viewing purposes. We extract the maximum wave-

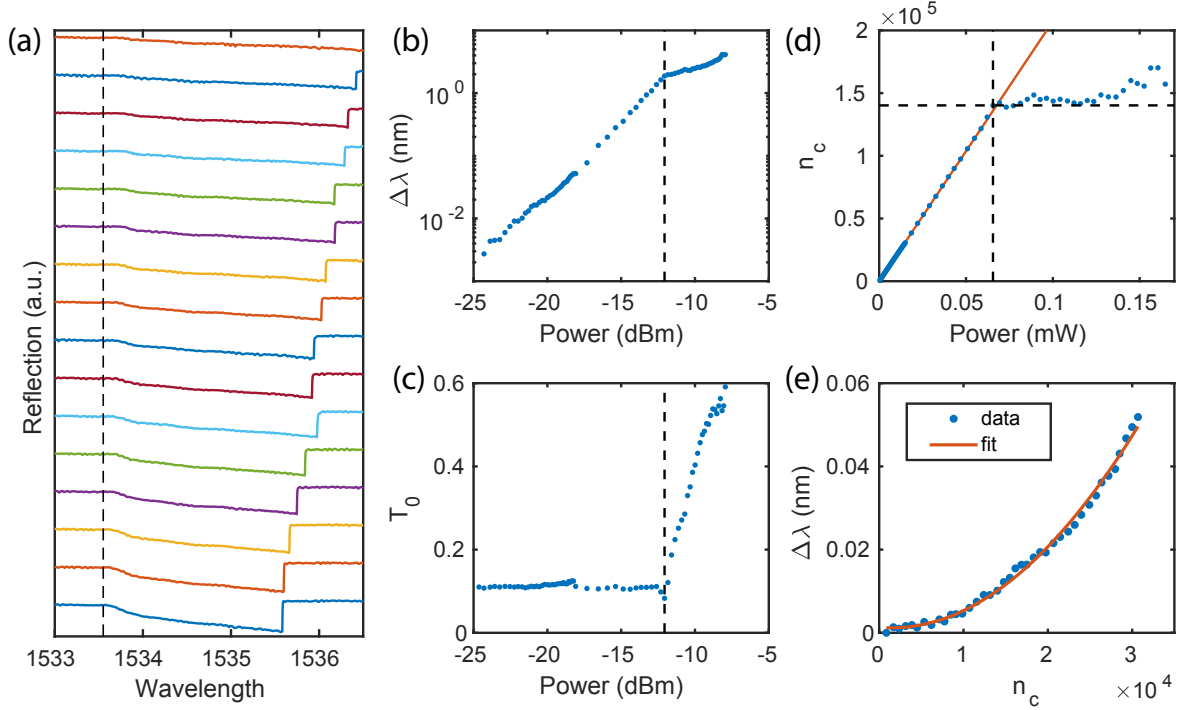


Fig. 9. Thermal-optical shift measurements. (a) Reflection signal of laser wavelength scan at increasing powers. Vertically displaced for viewing purposes. The vertical dashed line represents the cavity wavelength at low power. (b) Maximum optical cavity wavelength shift versus laser power, extracted from (a). (c) Minimum reflection T_0 at the resonance versus laser power, extracted from (a). (d) Maximal intracavity photon number versus laser power. (e) Wavelength shifts versus n_c before saturation (blue dots) and a quadratic fit (red line).

length shifts $\Delta\lambda_{\max}$ (fig. 9(b)) as well as minimum reflections at the resonance dip T_0 versus laser powers (fig. 9(c)). A sharp transition occurs near a threshold laser power $P_{\text{in,thres}} = 0.065$ mW. The wavelength shifts slow down and the transition dips get shallower.

With the coherent spectroscopy method, we confirmed that with powers $P_{\text{in}} > P_{\text{in,thres}}$ and n_c as high as 1.5×10^5 , the cavity linewidth stays roughly constant regardless of the increasing T_0 (see sec. C). Little additional loss is introduced by the high optical powers used in our measurements. We conclude that the increase in T_0 is due to an “early escape” of the mode, where $\Delta\lambda$ saturates and the cavity escapes back to far blue before the laser reaches the reflection dip. Based on measurements of the reflection dip $T_0 = |(i\Delta + \kappa/2 - \kappa_e)/(i\Delta + \kappa/2)|^2$, we could obtain the detuning Δ right before the mode escapes and calculate the corresponding intracavity photon number n_c . This n_c is the maximal intracavity photon number obtained for each laser power. The results are shown in fig. 9(d). For laser powers below $P_{\text{in,thres}}$, the maximal n_c grows linearly with respect to input powers. When n_c reaches $n_{c,\text{thres}} \sim 1.4 \times 10^5$ at $P_{\text{in}} = P_{\text{in,thres}}$, the intracavity photon numbers are observed to saturate at values near $n_{c,\text{thres}}$, largely deviating from the linear relation (red line) regardless of increasing laser powers. Similar threshold behaviors in terms of n_c were observed on different OMC devices and showed no obvious correlation with the optical quality factors. The physical mechanism leading to the threshold and the dependence of $n_{c,\text{thres}}$ on system parameters are not understood and will be the subject of further exploration.

For n_c smaller than the threshold, we plot the wavelength

shifts versus the intracavity photon numbers before $n_{c,\text{thres}}$ in fig. 9(e). A quadratic relationship between wavelength shift and intracavity photon number is obtained with $\Delta\lambda = \alpha_2 n_c^2$ where we call α_2 the quadratic thermal-induced cavity shift coefficient. $\alpha_2 \sim 6 \times 10^{-11}$ nm/(photon)² is obtained from the fit. The cavity shift could also be expressed in terms of frequency shift $\Delta\omega_c = \alpha_2 n_c^2$ where $\alpha_2 \sim -7$ Hz/(photon)². We observed that the measured $\Delta\lambda$ is well characterized by the quadratic fit for $10^4 \lesssim n_c \lesssim 10^5$ and deviates from the fit at low and high power, showing that the actual thermal-induced cavity shift has a complicated dependency on n_c , including a small linear n_c term and also terms with higher order. The quadratic contribution already dominates the wavelength shift when the shift is noticeable with $\Delta\lambda \gtrsim \kappa$, making the linear term difficult to measure.

B. Measurement of the thermal relaxation rate

In this section we consider the response of the cavity to a laser pump with slow and weak amplitude modulation. We first define related parameters and variables in Table 1. When referring to the steady-state values at a constant power, quantities are denoted with a bar.

We start by assuming a linear thermal-optical shift of the optical cavity frequency with respect to temperature change

$$\Delta\omega_c = C_0 \Delta T. \quad (11)$$

Then dynamics of the temperature change is modeled by

$$\frac{d\Delta T}{dt} = -\Gamma \Delta T + f(n_c), \quad (12)$$

Table 1. Definition of parameters related to thermal relaxation rate measurements.

Parameter	Description	Useful relation
P_{in}	input laser power	
ΔT	temperature change	
$\Delta\omega_c$	thermal-induced cavity shift	$\Delta\omega_c = \alpha_1 n_c + \alpha_2 n_c^2$
Δ	real-time cavity-laser detuning	$\Delta = \omega_c - \omega_l + \Delta\omega_c$
\dot{N}_{in}	input photon flux	$P_{\text{in}}/(\hbar\omega_l)$
n_c	intracavity photon number	$n_c = \kappa_e \dot{N}_{\text{in}}/(\Delta^2 + (\kappa/2)^2)$
δP_{in}	small laser power variation	
δn_c	small n_c variation due to δP_{in}	
$\delta\omega_c$	extra cavity shift variation due to δn_c	
$\delta\Delta$	small detuning variation	$\delta\Delta = \delta\omega_c$ for fixed laser wavelength
Γ	temperature relaxation rate	
Γ_2	measurement induced extra relaxation rate	
Γ_{tot}	total measured relaxation rate	$\Gamma_{\text{tot}} = \Gamma + \Gamma_2$

where $n_c = \kappa_e \dot{N}_{\text{in}}/(\Delta^2 + (\kappa/2)^2)$ is the instant intracavity photon number and $\dot{N}_{\text{in}} = P_{\text{in}}/(\hbar\omega_c)$ is the input photon flux of the pump. An exponential temperature relaxation with rate Γ is assumed. We also assume that the heating effect only directly depends on intracavity photon number n_c via a general function f . The dynamical equation could be formulated in terms of the cavity shift $\Delta\omega_c$ as

$$\frac{d\Delta\omega_c}{dt} = -\Gamma\Delta\omega_c + C_0 f(n_c). \quad (13)$$

This equation describes the complicated dynamics of $\Delta\omega_c$ which also enters $f(n_c)$ implicitly via n_c . C_0 can be absorbed into the function f so that f has the dimension of $(\text{rad/s})^2$. We will omit C_0 from now on. Note that eq. 13 gives the steady-state cavity shift $\bar{\Delta\omega}_c = f(\bar{n}_c)/\Gamma$ from which we could solve $\bar{\Delta\omega}_c$ and \bar{n}_c if f and Γ are known.

Based on eq. 13, we consider small time-dependent variations of laser power δP_{in} near the steady state solution. The laser wavelength is kept fixed. Note that n_c is a function of Δ and P_{in} so that

$$\frac{d\delta\Delta}{dt} = -\Gamma(\bar{\Delta\omega}_c + \delta\Delta) + f(\bar{n}_c) + f'(\bar{n}_c) \cdot \delta n_c \quad (14)$$

$$= -\Gamma\delta\Delta + f'(\bar{n}_c) \cdot \left(\frac{\bar{n}_c \delta P_{\text{in}}}{P_{\text{in}}} - \frac{2\bar{n}_c \bar{\Delta} \delta\Delta}{\bar{\Delta}^2 + (\kappa/2)^2} \right) \quad (15)$$

$$= -(\Gamma + \Gamma_2)\delta\Delta + f'(\bar{n}_c) \bar{n}_c \cdot \frac{\delta P_{\text{in}}}{P_{\text{in}}}, \quad (16)$$

where

$$\Gamma_2 = \frac{2\bar{\Delta}}{\bar{\Delta}^2 + (\kappa/2)^2} \cdot f'(\bar{n}_c) \bar{n}_c = g(\bar{\Delta}) \cdot h(\bar{n}_c). \quad (17)$$

The extra relaxation rate Γ_2 reflects the fact that the laser amplitude-modulation measurement method enters the complicated dynamics of the system itself, leading to an effective relaxation rate in addition to the actual relaxation rate Γ . We define functions g and h to represent the dependency of Γ_2 on

$\bar{\Delta}$ and \bar{n}_c . We point out that $\bar{\Delta}$ and \bar{n}_c can be independently controlled by preparing the steady state with different laser frequencies ω_l and powers P_{in} .

When the input laser power has a small variation $\delta P_{\text{in}} = a \cos(\omega t)$, by assuming $\delta\Delta = \beta \cos(\omega t + \phi)$ and plugging into eq. 16, we get the amplitude response of $\delta\Delta$ to δP_{in} to be

$$\left| \frac{\beta}{a} \right| \propto \frac{1}{\sqrt{\omega^2 + (\Gamma + \Gamma_2)^2}}. \quad (18)$$

As a result, the total ‘‘relaxation rate’’ $\Gamma_{\text{tot}} = \Gamma + \Gamma_2$ can be measured from the low-frequency amplitude response of $\delta\Delta$. With the measurement of Γ_{tot} and independent control over $\bar{\Delta}$ and \bar{n}_c , we are allowed to probe the structure of Γ_2 and thus the unknown function f .

Proceeding to the determination of f , we assume a polynomial form $f(n) = a_1 n + a_2 n^2 + O(n^3)$, where higher order terms are assumed to be small based on the steady-state cavity shift measurements. With this assumption, $h(n) = n f'(n) = a_1 n + 2a_2 n^2$, and

$$\Gamma_{\text{tot}} = (1, g(\bar{\Delta})\bar{n}_c, 2g(\bar{\Delta})\bar{n}_c^2) \cdot (\Gamma, a_1, a_2)^T = \mathbf{M} \cdot \mathbf{b}. \quad (19)$$

By carrying out multiple measurements of Γ_{tot} with different \mathbf{M} , the thermal relaxation rate Γ and coefficients a_1 and a_2 can be determined by solving a linear regression problem. Once Γ, a_1 and a_2 are obtained, the steady-state cavity shift is $\bar{\Delta\omega}_c = \alpha_1 \bar{n}_c + \alpha_2 \bar{n}_c^2 = a_1 \bar{n}_c / \Gamma + a_2 \bar{n}_c^2 / \Gamma$.

We now show that the response of $\delta\Delta$ can be directly measured by the same coherent spectroscopy setup at low modulation frequencies. When there is no slow thermal-induced cavity wavelength shift, the optical response is given by

$$r(\omega \ll \Delta) \approx 1 - \frac{\kappa_e}{i(\Delta - \omega) + \kappa/2}. \quad (20)$$

When the slow cavity wavelength shift is considered, Δ is replaced by $\bar{\Delta} + \delta\Delta(\omega)$, where $\delta\Delta(\omega)$ is the frequency-domain response of the slow thermal-induced wavelength shift. For

small and low-frequency intensity modulation, we assume $\omega \ll \delta\Delta \ll \Delta$, and the response can be simplified as

$$r(\omega \ll \Delta) \approx 1 - \frac{\kappa_e}{i(\Delta + \delta\Delta(\omega)) + \kappa/2} \quad (21)$$

$$\approx 1 - \frac{\kappa_e}{i\Delta + \kappa/2} + \frac{\kappa_e}{i\Delta + \kappa/2} \cdot \frac{i\delta\Delta(\omega)}{i\Delta + \kappa/2}. \quad (22)$$

The resulting intensity response is

$$|r(\omega \ll \Delta)|^2 = A + B \cdot \delta\Delta(\omega) + O\left(\left(\frac{\delta\Delta}{\Delta}\right)^2\right), \quad (23)$$

where A and B are two real-valued functions of Δ , κ and κ_e . The exact forms of A and B are involving but not important since they are approximately independent of frequency for $\omega \ll \Delta$. As a result, for low frequency intensity modulation, the only frequency-dependent intensity response is from the variation of thermal-induced cavity shift $\delta\Delta = \delta\omega_c$.

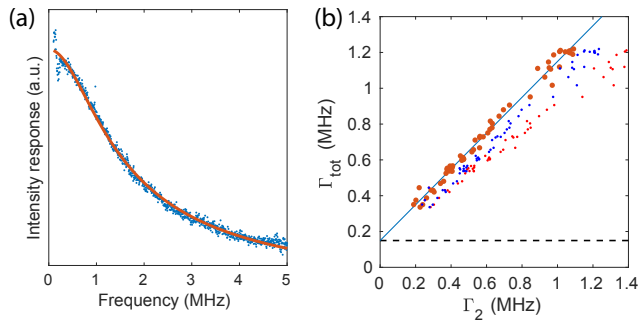


Fig. 10. Measurement of thermal relaxation rate. (a) Example of low frequency intensity modulation response of the OMC system. Blue: data. Red: Lorentzian fit. (b) Measured total relaxation rate versus measurement induced extra relaxation rate (orange). The black dashed line shows the actual thermal relaxation rate of the OMC. The blue line is a guide for the eye and has a slope of 1.

We measured the intensity response $|r(\omega \ll \Delta)|^2$ for frequency range 100 kHz \sim 5 MHz. The amplitude of the response is fitted to a Lorentzian centered at frequency $f = 0$. The linewidth of this Lorentzian corresponds to the total relaxation rate Γ_{tot} . A typical low frequency response is shown in fig. 10(a) with the Lorentzian fit (red). In this way we extracted Γ_{tot} under different laser powers and wavelengths. The steady-state cavity-laser detuning $\bar{\Delta}$ is measured at the same time by an optical sideband sweep across the cavity. With measured Γ_{tot} , $\bar{\Delta}$ and \bar{n}_c , the linear regression problem eq. 19 is solved. We obtain the true thermal relaxation rate $\Gamma = 150$ kHz, linear thermal-induced cavity shift coefficient $\alpha_1 = a_1/\Gamma \approx -7.1 \times 10^4$ Hz/photon and quadratic thermal-induced cavity shift coefficient $\alpha_2 = a_2/\Gamma \approx -1.5$ Hz/(photon)².

The thermal relaxation rate Γ quantitatively agrees with the thermal-optical response time scale of ~ 10 μ s reported in Ref. [62] and is slightly faster due to smaller device volume. We note that for $n_c \gtrsim 5 \times 10^4$, the thermal-optical shift starts to be dominated by the quadratic contribution, which agrees with the steady-state wavelength shift measurement in the last section. We note that the α_2 obtained here is smaller than the value from steady-state wavelength shift measurement by a factor ~ 4 .

We further calculated Γ_2 with a_1 and a_2 from the linear regression and n_c from the measurements. We show in fig. 10(b) the

measured Γ_{tot} versus calculated Γ_2 (orange dots). The horizontal black dashed line corresponds to the constant Γ . A blue line starting at $(0, \Gamma)$ with slope equals to one is plotted for guide of the eye. It's clear that good agreement is obtained between the linear regression results and the equation $\Gamma_{\text{tot}} = \Gamma + \Gamma_2$, under a large variation of both laser powers and cavity-laser detunings. To show the reliability of the linear regression results, we manually increase the obtained value of a_1 (a_2) by 50% and plot the modified Γ_2 in fig. 10(b) as small blue (red) dots for comparison. Deviation from $\Gamma_{\text{tot}} = \Gamma + \Gamma_2$ can be clearly observed.

C. MEASUREMENT OF OPTICAL LINEWIDTH WITH DIFFERENT INTRACAVITY PHOTON NUMBERS

In sec. BA we observed the minimal transmission T_0 increased for high laser powers. We further deduced the minimal cavity-laser detunings before the optical mode jumped back to the blue side of the laser based on the minimal transmission measurements. However, a change in the cavity intrinsic linewidth κ_i could also change the transmission dip, where $T_0|_{\Delta=0} = |(\kappa/2 - \kappa_e)/(\kappa/2)|^2 = |(\kappa_i - \kappa_e)/(\kappa_i + \kappa_e)|^2$. To track any considerable change in the cavity intrinsic linewidth, we fit the probe response from the coherent spectroscopy with different pump laser powers and different cavity-laser detunings. This two-tone spectroscopy effectively gives us the linear response of the cavity at different pump powers and helps us determine Δ , κ_e , and κ_i , as a function of laser power and detuning.

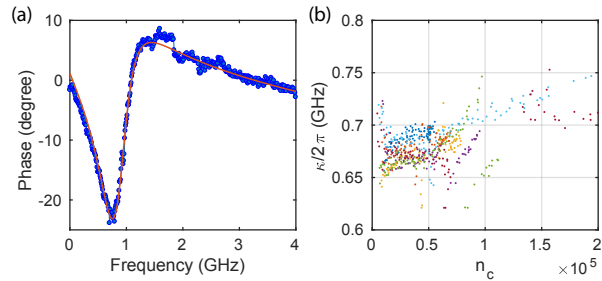


Fig. 11. Measurement of optical linewidth κ with different intracavity photon numbers n_c . (a) A typical phase response of the probe with a high pump power $P_{\text{in}} \sim 0.2$ mW and a near-cavity detuning $\Delta \sim \kappa$. The red line shows the fit result. (b) Extracted total optical linewidth κ versus different intracavity photon numbers n_c under different pump powers and detunings. Different colors correspond to different pump laser powers.

Fig. 11(a) shows one typical phase response of the probe with a high pump laser power $P_{\text{in}} = 0.21$ mW and a small cavity-laser detuning $\Delta \sim -\kappa$. By fitting the phase response (red), we extract the total optical linewidth κ . Measurements of κ versus intracavity photon numbers n_c with various pump powers and detunings are plotted in fig. 11(b). Different colors correspond to different pump laser powers ranging from 96 μ W to 0.21 mW. We obtained $\kappa \approx 0.7$ GHz with relative standard deviation $\sim 9\%$ for all measurements with different pump powers. A linear increase in total linewidth for increasing n_c can be observed and shows different slopes for different pump powers. We note that in general the optical linewidth varies by less than 15% for n_c varying more than two orders of magnitude.

D. COUPLING AND CONVERSION BETWEEN MICROWAVE, MECHANICS AND OPTICS

A. Input-output formalism of a optomechanical crystal coupling to a microwave resonator or a microwave channel

Consider a system with an OMC coupling to a microwave resonator c with coupling strength g_μ . We start by writing down the frequency-domain Heisenberg-Langevin equations of motion in a rotating frame at the laser frequency for $\Delta \sim \omega_m$:

$$-i\omega a(\omega) = -(i\Delta + \frac{\kappa}{2})a - iGb - \sqrt{\kappa_e}a_{in} \quad (24)$$

$$-i\omega b(\omega) = -(i\omega_m + \frac{\gamma}{2})b - iGa - ig_\mu c - \sqrt{\gamma_e}b_{in} \quad (25)$$

$$-i\omega c(\omega) = -(i\omega_\mu + \frac{\kappa_\mu}{2})c - ig_\mu b - \sqrt{\kappa_{\mu,e}}c_{in} \quad (26)$$

We assume that every mode is coupled to a single external channel respectively. The counter-rotating terms have been omitted for simplicity. We introduce short-hands

$$A_a = i(\Delta - \omega) + \kappa/2 \quad (27)$$

$$A_b = i(\omega_m - \omega) + \gamma/2 \quad (28)$$

$$A_c = i(\omega_\mu - \omega) + \kappa_\mu/2 \quad (29)$$

$$\eta_{ab} = -iG/A_a \quad (30)$$

$$\eta_{ba} = -iG/A_b \quad (31)$$

$$\eta_{bc} = -ig/A_b \quad (32)$$

$$\eta_{cb} = -ig/A_c \quad (33)$$

$$\eta_{ijk} = \eta_{ij}\eta_{jk} \quad (34)$$

where i, j, k run through a, b, c . With them the solution can be expressed as

$$\begin{bmatrix} a \\ b \\ c \end{bmatrix} = \frac{1}{1 - \eta_{aba} - \eta_{bcb}} \begin{bmatrix} 1 - \eta_{bcb} & \eta_{ab} & \eta_{abc} \\ \eta_{ba} & 1 & \eta_{bc} \\ \eta_{cba} & \eta_{cb} & 1 - \eta_{aba} \end{bmatrix} \begin{bmatrix} -\frac{\sqrt{\kappa_e}a_{in}}{A_a} \\ -\frac{\sqrt{\gamma_e}b_{in}}{A_b} \\ -\frac{\sqrt{\kappa_{\mu,e}}c_{in}}{A_c} \end{bmatrix} \quad (35)$$

From eq. 35, we can directly read the electro-optic conversion S parameters when only input c_{in} or a_{in} presents:

$$S_{ac} \equiv \frac{a_{out}}{c_{in}} = \frac{\sqrt{\kappa_e}a}{c_{in}} \quad (36)$$

$$= \sqrt{\kappa_e} \frac{\eta_{abc}}{1 - \eta_{aba} - \eta_{bcb}} \frac{-\sqrt{\kappa_{\mu,e}}}{A_c} \quad (37)$$

$$= \sqrt{\kappa_e} \frac{1}{A_a} \frac{Gg_\mu}{A_b + G^2/A_a + g_\mu^2/A_c} \frac{1}{A_c} \sqrt{\kappa_{\mu,e}} \quad (38)$$

$$= S_{ca} \equiv \frac{c_{out}}{a_{in}} \quad (39)$$

At perfectly matched frequencies $\omega = \Delta = \omega_m = \omega_\mu$, we have the conversion efficiency

$$\eta \equiv |S_{ac}|^2 = |S_{ca}|^2 \quad (40)$$

$$= \kappa_e \frac{4}{\kappa^2} \frac{4G^2g_\mu^2/\gamma^2}{(1 + 4G^2/\kappa\gamma + 4g_\mu^2/\kappa_\mu\gamma)^2} \frac{4}{\kappa_\mu^2} \kappa_{\mu,e} \quad (41)$$

$$= \eta_{ext,a}\eta_{ext,c} \frac{4C_{ab}C_{bc}}{(1 + C_{ab} + C_{bc})^2} \quad (42)$$

where $\eta_{ext,a} = \kappa_e/\kappa$ and $\eta_{ext,c} = \kappa_{\mu,e}/\kappa_\mu$ are defined as the external efficiencies. C_{ab} (C_{bc}) is the cooperativity between the mechanical mode and the optical (microwave) mode. The

maximal conversion efficiency $\eta = \eta_{ext,a}\eta_{ext,c}$ is achieved for $C_{ab} = C_{bc} \gg 1$.

We proceed to consider the simplified case where the mechanical mode is directly coupled to a microwave channel. The external decay rate γ_e now represents the coupling between the microwave channel and the mechanical mode. The equations of motion read

$$-i\omega a(\omega) = -(i\Delta + \frac{\kappa}{2})a - iGb - \sqrt{\kappa_e}a_{in} \quad (43)$$

$$-i\omega b(\omega) = -(i\omega_m + \frac{\gamma}{2})b - iGa - \sqrt{\gamma_e}c_{in} \quad (44)$$

and the simplified version of eq. 35 is

$$\begin{bmatrix} a \\ b \end{bmatrix} = \frac{1}{1 - \eta_{aba}} \begin{bmatrix} 1 & \eta_{ab} \\ \eta_{ba} & 1 \end{bmatrix} \begin{bmatrix} -\frac{\sqrt{\kappa_e}a_{in}}{A_a} \\ -\frac{\sqrt{\gamma_e}c_{in}}{A_b} \end{bmatrix}. \quad (45)$$

Similarly, the electro-optic S parameter is

$$S_{ac} = \sqrt{\kappa_e} \frac{\eta_{ab}}{1 - \eta_{aba}} \frac{-\sqrt{\gamma_e}}{A_b} \quad (46)$$

$$= \sqrt{\kappa_e} \frac{1}{A_a} \frac{iG}{A_b + G^2/A_a} \sqrt{\gamma_e} \quad (47)$$

The resulting conversion efficiency at perfectly-matched frequency $\omega = \Delta = \omega_m$ is

$$\eta = \kappa_e \frac{4}{\kappa^2} \frac{4G^2/\gamma^2}{(1 + 4G^2/\kappa\gamma)^2} \gamma_e \quad (48)$$

$$= \eta_{ext,a}\eta_{ext,b} \frac{4C_{ab}}{(1 + C_{ab})^2} \quad (49)$$

where $\eta_{ext,b} = \gamma_e/\gamma$. The maximum of conversion efficiency occurs at the matching condition $C_{ab} = 1$, where similarly $\eta = \eta_{ext,a}\eta_{ext,b}$.

B. Measurement of coupling between the mechanical resonator and a microwave channel

Our OMC can be coupled to a microwave channel via the piezoelectric interaction. We evaporated electrode on both ends of the nanobeam and connected them to a transmission line with impedance $Z_0 = 50 \Omega$. The electric field generated by the electrode is parallel to the nanobeam. The same configuration can also be adopted for coupling the mechanical resonator to microwave circuits.

From the last section, with $\Delta = \omega_m$, the coherent mechanical field amplitude is

$$\beta = \frac{-\sqrt{\gamma_e}c_{in}}{i(\omega_m - \omega_\mu) + \gamma_{tot}/2}, \quad (50)$$

where c_{in} is the input microwave amplitude with a unit of $1/\sqrt{\text{Hz}}$, $\gamma_{tot} = \gamma_i + \gamma_e + \gamma_{OM}$ is the total mechanical linewidth and $\omega_\mu \approx \omega_m$ is the microwave signal frequency. The resulting coherent phonon number in the mechanical mode is

$$n_{coh} = |\beta|^2 = \frac{\gamma_e \dot{N}_\mu}{(\omega_\mu - \omega_m)^2 + (\gamma_{tot}/2)^2}, \quad (51)$$

where $\dot{N}_\mu = |c_{in}|^2 = \eta_{loss} P_\mu / (\hbar\omega_\mu)$ is the input microwave photon flux, P_μ is the output power of the VNA and $\eta_{loss} \approx 58\%$ accounts for external RF cable loss. We tune $\omega_\mu = \omega_m$ and measure the transduced optical sideband power spectral density

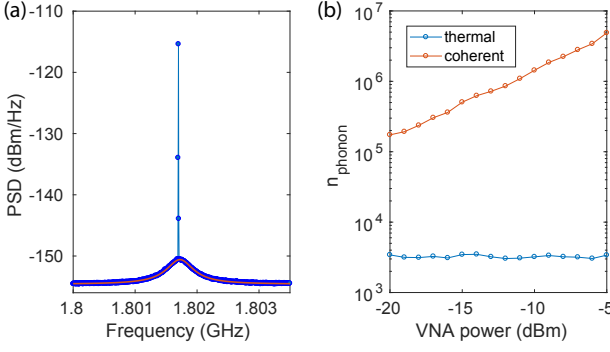


Fig. 12. Microwave to mechanics conversion. (a) Measured power spectral density of thermal mechanical motion and coherent mechanical motion from the piezoelectric drive. Blue: data, red: Lorentzian fit of the thermal motion peak. (b) Extracted phonon numbers from the power spectral density for different VNA drive power.

of both the coherent phonons and thermal phonons using the RSA. The microwave-to-mechanics coupling rate is given by

$$\gamma_e = \frac{n_{\text{coh}} \gamma_{\text{tot}}^2}{4\dot{N}_\mu}. \quad (52)$$

Fig. 12(a) shows a measured optical sideband power spectral density (PSD). The thermal mechanical motion give rise to the broad Lorentzian peak and the coherent RF drive corresponds to the sharp peak. We integrate the sideband RF power under both the thermal peak P_{therm} and the coherent peak P_{coh} independently. The thermal occupancy of the mechanical mode is calculated by $n_{\text{therm}} = k_B T / \hbar \omega_m \approx 3400$ with $T = 295$ K. The optical and electrical gain of the whole readout chain is then determined by $G = \langle P_{\text{therm}} \rangle / n_{\text{therm}}$ for a certain optical pump power. We drive the OMC with different RF powers and extract the thermal and coherent phonon numbers from the PSD in fig. 12(b). The coherent phonon numbers rise linearly with the increasing RF powers while the thermal phonon occupancies stay near-constant. We obtained $\gamma_e / 2\pi = 8.8 \pm 0.56$ mHz.

C. Estimating coupling between the LN OMC and a microwave resonator or a superconducting qubit

In this section we estimate the coupling of the mechanical mode to a microwave resonator or a superconducting qubit based on our measurement of γ_e in the last section.

The mechanical resonator is commonly modeled as a parallel LC resonator [25]. To take into account the non-zero energy decay rate γ , a resistor is added in parallel such that $\gamma = 1/(RC)$. The mechanical resonator can be coupled to an external 50Ω transmission line through coupling capacitance C_g , as shown in fig. 13(a). The external coupling introduces a frequency shift and an additional decay rate from an effective conductance $1/Z_e = \omega_m^2 C_g^2 Z_0$ [63]. From this equivalence, we obtain a relationship between the coupling capacitance C_g and the coupling induced decay rate $\gamma_e = \omega_m^2 C_g^2 Z_0 / C$.

We show in fig. 13(e) a mechanical resonator coupling to a microwave resonator or a superconducting qubit. The coupling

rate is given by [64]

$$g \approx \sqrt{\omega_m \omega_2} \cdot \frac{C_g}{2\sqrt{(C + C_g)(C_2 + C_g)}} \quad (53)$$

$$\approx \sqrt{\omega_m \omega_2} \cdot \frac{C_g}{2\sqrt{C C_2}}, \quad (54)$$

where we've made the assumption that $C_g \ll C_1, C_2$. To simplify the result, we assume that the two modes are perfectly matched with $\omega_2 = \omega_m$, and the microwave resonator has a characteristic impedance $Z_c = \sqrt{L_2 / C_2}$. As a result,

$$g^2 = \frac{\omega_m^2 C_g^2}{C} \cdot \frac{1}{4C_2} = \frac{\gamma_e}{Z_0} \cdot \frac{\omega_m Z_c}{4}, \quad (55)$$

where we made the substitution $1/C_2 = \omega_2 Z_c$.

In conclusion, the coupling rate between a mechanical resonator and a microwave channel γ_e and the coupling rate between a mechanical resonator and a microwave resonator g are related by $g = \sqrt{\gamma_e \omega_m} \sqrt{Z_c / Z_0} / 2$.

E. EXTRACTING PUMP DETUNINGS FROM ON-CHIP ELECTRO-OPTIC MODULATION

We start with the electro-optic interaction Hamiltonian. The perturbation on the optical mode frequency from a voltage V across the electrodes are modeled by

$$H_{\text{EO}} = \hbar \frac{d\omega}{dV} V \hat{a}^\dagger \hat{a} \quad (56)$$

$$= -i\hbar \sqrt{\kappa_{e,\mu}} \hat{a}^\dagger \hat{a} (c_{\text{in}} - c_{\text{in}}^\dagger). \quad (57)$$

Where we rewrite the voltage in terms of input microwave amplitude c_{in} and choose a specific phase of c_{in} for later convenience. After linearization and rotating wave approximation:

$$H_{\text{EO}} = -i\hbar \sqrt{\kappa_{e,\mu}} (\alpha_0 \hat{a}^\dagger c_{\text{in}} - \alpha_0^* \hat{a} c_{\text{in}}^\dagger). \quad (58)$$

where $\alpha_0 = -\sqrt{\kappa_e} \alpha_{\text{in}} / (i\Delta + \kappa/2)$ is the optical intracavity pump amplitude and α_{in} is the pump input photon amplitude. Equation of motion for the optical sideband amplitude is

$$-i\omega a(\omega) = -(i\Delta + \frac{\kappa}{2})a - \sqrt{\kappa_{e,\mu}} \alpha_0 c_{\text{in}} \quad (59)$$

from which we could solve the sideband amplitude and calculate the output optical field as

$$\begin{aligned} \alpha_{\text{out}} &= \left[1 - \frac{\kappa_e}{i\Delta + \frac{\kappa}{2}} \left(1 - \frac{\sqrt{\kappa_{e,\mu}}}{i(\Delta - \omega_\mu) + \frac{\kappa}{2}} c_{\text{in}} e^{-i\omega_\mu t} \right) \right] \alpha_{\text{in}} \\ &= \left(r(\Delta) + s_{\text{EO}}(\omega_\mu, \Delta) c_{\text{in}} e^{-i\omega_\mu t} \right) \alpha_{\text{in}}, \end{aligned} \quad (60)$$

where

$$r(\Delta) = 1 - \frac{\kappa_e}{i\Delta + \kappa/2}, \quad (61)$$

$$s_{\text{EO}}(\omega, \Delta) = \frac{\kappa_e}{i\Delta + \kappa/2} \frac{\sqrt{\kappa_{e,\mu}}}{i(\Delta - \omega) + \frac{\kappa}{2}}. \quad (62)$$

The electronic signal from the high-speed photo-detector is

$$\begin{aligned} V_{\text{HS}} &= G |\alpha_{\text{out}}|^2 = G |\alpha_{\text{in}}|^2 \left(|r(\Delta)|^2 + \right. \\ &\quad \left. r^*(\Delta) s_{\text{EO}}(\omega_\mu, \Delta) c_{\text{in}} e^{-i\omega_\mu t} + h.c. + O(c_{\text{in}}^2) \right) \end{aligned} \quad (63)$$

where G denotes the total detection gain. As a result, the VNA directly measures $S_{21}(\omega, \Delta) \propto G |\alpha_{\text{in}}|^2 r^*(\Delta) s_{\text{EO}}(\omega, \Delta) S_{\text{ext}}(\omega)$

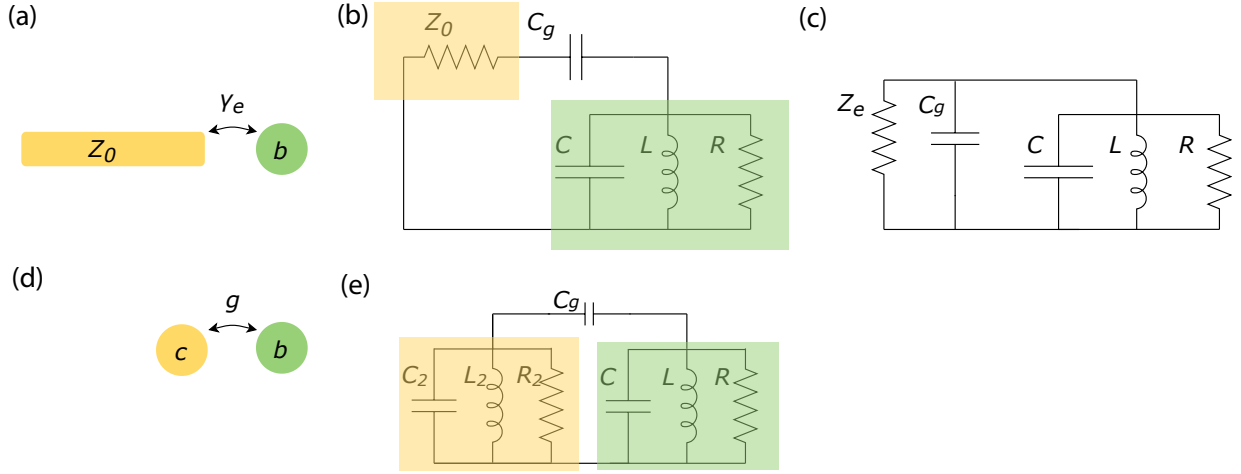


Fig. 13. Coupling between mechanics and microwave. (a) A mechanical resonator (green) coupled to a microwave channel (yellow). (b) Circuit model of (a). (c) Equivalent circuit of (b). (d) A mechanical resonator (green) coupled to a microwave resonator (yellow). (e) Circuit model of (d).

where we further include the external response of the cables and wirebonds in $S_{\text{ext}}(\omega)$.

For the coherent spectroscopy, the external response and the detection gain can be removed by dividing the response with a background taken with far-detuned pump laser [9, 65]. The electro-optic (EO) sideband is generated by the EOM and doesn't depend on the cavity-laser detuning. However, for the on-chip EO modulation, the intracavity photon numbers are much smaller for far-detuned pump laser, resulting in a much weaker EO sideband and a very low SNR. To eliminate the detection gain G and the external response, we take the ratio between two S_{21} measurements with different near-cavity detunings Δ_1 and Δ_2 where $|\Delta_1 - \Delta_2| \gtrsim \kappa$. The gain and external response is identical and cancels, leaving only the ratio of the on-chip EO response. We denote the ratio of the S_{21} as

$$S_{\Delta_2/\Delta_1}(\omega) = \frac{r^*(\Delta_2)s_{\text{EO}}(\omega, \Delta_2)}{r^*(\Delta_1)s_{\text{EO}}(\omega, \Delta_1)}. \quad (64)$$

By fitting the measured S_{21} ratio with different detunings and identical pump laser power, we extract both detunings Δ_1 and Δ_2 .

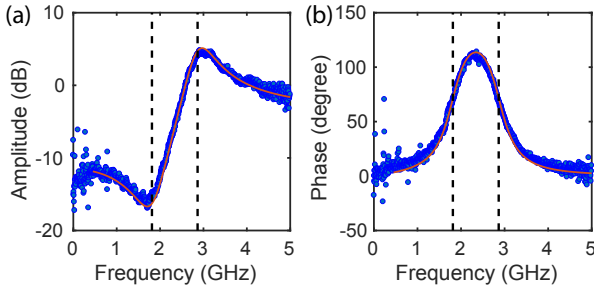


Fig. 14. On-chip electro-optic response and fit. (a) Amplitude and (b) phase of the electro-optic response. Red curves show the fitting results. The detunings extracted from the fit are shown as black vertical dashed lines for comparison.

In fig. 14 we show a typical measured S_{Δ_2/Δ_1} (blue) and the fitting results using eq. 64 (red). The external responses are

perfectly removed, allowing us to extract the detunings of the pump laser. We point out that with the piezoelectric drive off, the pump detunings could also be extracted using the external EOM sideband sweep as used in the coherent spectroscopy.

F. ROTATED PHOTOELASTIC TENSOR COMPONENTS

The original photoelastic tensor components are given by [66]

$$p = \begin{bmatrix} p_{11} & p_{12} & p_{13} & p_{14} & 0 & 0 \\ p_{12} & p_{11} & p_{13} & -p_{14} & 0 & 0 \\ p_{31} & p_{31} & p_{33} & 0 & 0 & 0 \\ p_{41} & -p_{41} & 0 & p_{44} & 0 & 0 \\ 0 & 0 & 0 & 0 & p_{44} & p_{41} \\ 0 & 0 & 0 & 0 & p_{14} & (p_{11} - p_{12})/2 \end{bmatrix}. \quad (65)$$

Using the rotation matrix and MATHEMATICA [67], we obtain the rotated photoelastic components in the contracted index notation for X-cut LN as

$$p'_{\text{LNX}} = \begin{bmatrix} p'_{11} & p'_{12} & p'_{13} & 0 & 0 & p'_{16} \\ p'_{21} & p'_{22} & p'_{23} & 0 & 0 & p'_{26} \\ p'_{31} & p'_{32} & p'_{33} & 0 & 0 & p'_{36} \\ 0 & 0 & 0 & p'_{44} & p'_{45} & 0 \\ 0 & 0 & 0 & p'_{54} & p'_{55} & 0 \\ p'_{61} & p'_{62} & p'_{63} & 0 & 0 & p'_{66} \end{bmatrix}, \quad (66)$$

with

$$p'_{11} = p_{11} \sin^4(\phi) + p_{44} \sin^2(2\phi) + p_{33} \cos^4(\phi) + p_{13} \sin^2(\phi) \cos^2(\phi) + p_{31} \sin^2(\phi) \cos^2(\phi) - 2p_{14} \sin^3(\phi) \cos(\phi) - 2p_{41} \sin^3(\phi) \cos(\phi), \quad (67)$$

$$p'_{12} = p_{13} \sin^4(\phi) - p_{44} \sin^2(2\phi) + p_{31} \cos^4(\phi) - 2p_{41} \sin(\phi) \cos^3(\phi) + p_{11} \sin^2(\phi) \cos^2(\phi) + p_{33} \sin^2(\phi) \cos^2(\phi) + 2p_{14} \sin^3(\phi) \cos(\phi) \quad (68)$$

$$p'_{13} = p_{12} \sin^2(\phi) + p_{41} \sin(2\phi) + p_{31} \cos^2(\phi) \quad (69)$$

$$p'_{16} = \sin(\phi) \left(-p_{31} \cos^3(\phi) + p_{33} \cos^3(\phi) - 2p_{44} \cos(2\phi) \cos(\phi) + 2p_{41} \sin(\phi) \cos^2(\phi) - p_{11} \sin^2(\phi) \cos(\phi) + p_{13} \sin^2(\phi) \cos(\phi) + p_{14} \sin(\phi) \cos(2\phi) \right) \quad (70)$$

$$p'_{21} = p_{31} \sin^4(\phi) - p_{44} \sin^2(2\phi) + p_{13} \cos^4(\phi) - 2p_{14} \sin(\phi) \cos^3(\phi) + p_{11} \sin^2(\phi) \cos^2(\phi) + p_{33} \sin^2(\phi) \cos^2(\phi) + 2p_{41} \sin^3(\phi) \cos(\phi) \quad (71)$$

$$p'_{22} = p_{33} \sin^4(\phi) + p_{44} \sin^2(2\phi) + p_{11} \cos^4(\phi) + 2p_{14} \sin(\phi) \cos^3(\phi) + 2p_{41} \sin(\phi) \cos^3(\phi) + p_{13} \sin^2(\phi) \cos^2(\phi) + p_{31} \sin^2(\phi) \cos^2(\phi) \quad (72)$$

$$p'_{23} = p_{12} \cos^2(\phi) + \sin(\phi) (p_{31} \sin(\phi) - 2p_{41} \cos(\phi)) \quad (73)$$

$$p'_{26} = \cos(\phi) \left(-p_{31} \sin^3(\phi) + p_{33} \sin^3(\phi) + p_{14} \cos(\phi) \cos(2\phi) - p_{11} \sin(\phi) \cos^2(\phi) + p_{13} \sin(\phi) \cos^2(\phi) - 2p_{41} \sin^2(\phi) \cos(\phi) + 2p_{44} \sin(\phi) \cos(2\phi) \right) \quad (74)$$

$$p'_{31} = p_{12} \sin^2(\phi) + p_{14} \sin(2\phi) + p_{13} \cos^2(\phi) \quad (75)$$

$$p'_{32} = p_{12} \cos^2(\phi) + \sin(\phi) (p_{13} \sin(\phi) - 2p_{14} \cos(\phi)) \quad (76)$$

$$p'_{33} = p_{11} \quad (77)$$

$$p'_{36} = \frac{1}{2} (p_{12}(-\sin(2\phi)) + p_{13} \sin(2\phi) - 2p_{14} \cos(2\phi)) \quad (78)$$

$$p'_{44} = \frac{1}{2} (p_{11} - p_{12}) \cos^2(\phi) - p_{14} \sin(\phi) \cos(\phi) + \sin(\phi) (p_{44} \sin(\phi) - p_{41} \cos(\phi)) \quad (79)$$

$$p'_{45} = \sin(\phi) (p_{41} \sin(\phi) + p_{44} \cos(\phi)) - \cos(\phi) \left(\frac{1}{2} (p_{11} - p_{12}) \sin(\phi) + p_{14} \cos(\phi) \right) \quad (80)$$

$$p'_{54} = \sin(\phi) \left(p_{14} \sin(\phi) - \frac{1}{2} (p_{11} - p_{12}) \cos(\phi) \right) + \cos(\phi) (p_{44} \sin(\phi) - p_{41} \cos(\phi)) \quad (81)$$

$$p'_{55} = \sin(\phi) \left(\frac{1}{2} (p_{11} - p_{12}) \sin(\phi) + p_{14} \cos(\phi) \right) + \cos(\phi) (p_{41} \sin(\phi) + p_{44} \cos(\phi)) \quad (82)$$

$$p'_{61} = \sin(\phi) \left(-p_{41} \sin^3(\phi) + p_{44} \sin(\phi) \sin(2\phi) - p_{13} \cos^3(\phi) + p_{33} \cos^3(\phi) - 2p_{44} \cos^3(\phi) + 2p_{14} \sin(\phi) \cos^2(\phi) \right. \\ \left. + p_{41} \sin(\phi) \cos^2(\phi) - p_{11} \sin^2(\phi) \cos(\phi) + p_{31} \sin^2(\phi) \cos(\phi) \right) \quad (83)$$

$$p'_{62} = \cos(\phi) \left(p_{33} \sin^3(\phi) + p_{31} \sin(\phi) \cos^2(\phi) + \cos^2(\phi) (2p_{44} \sin(\phi) + p_{41} \cos(\phi)) \right. \\ \left. - \sin(\phi) (p_{11} \cos^2(\phi) + \sin(\phi) (p_{13} \sin(\phi) + 2p_{44} \sin(\phi) + 2p_{14} \cos(\phi) + p_{41} \cos(\phi))) \right) \quad (84)$$

$$p'_{63} = \frac{1}{2} (p_{12}(-\sin(2\phi)) + p_{31} \sin(2\phi) - 2p_{41} \cos(2\phi)) \quad (85)$$

$$p'_{66} = \frac{1}{8} \left(2p_{11} \sin^2(2\phi) - 2p_{14} \sin(4\phi) - 2p_{41} \sin(4\phi) + p_{13}(\cos(4\phi) - 1) + p_{31} \cos(4\phi) \right. \\ \left. - p_{33} \cos(4\phi) + 4p_{44} \cos(4\phi) - p_{31} + p_{33} + 4p_{44} \right) \quad (86)$$

For Y-cut LN, the rotated photoelastic tensor components are given by

$$p'_{\text{LNY}} = \begin{bmatrix} p'_{11} & p'_{12} & p'_{13} & p'_{14} & p'_{15} & p'_{16} \\ p'_{21} & p'_{22} & p'_{23} & p'_{24} & p'_{25} & p'_{26} \\ p'_{31} & p'_{32} & p'_{33} & p'_{34} & p'_{35} & p'_{36} \\ p'_{41} & p'_{42} & p'_{43} & p'_{44} & p'_{45} & p'_{46} \\ p'_{51} & p'_{52} & p'_{53} & p'_{54} & p'_{55} & p'_{56} \\ p'_{61} & p'_{62} & p'_{63} & p'_{64} & p'_{65} & p'_{66} \end{bmatrix}, \quad (87)$$

where

$$p'_{11} = p_{11} \sin^4(\phi) + p_{44} \sin^2(2\phi) + p_{33} \cos^4(\phi) + p_{13} \sin^2(\phi) \cos^2(\phi) + p_{31} \sin^2(\phi) \cos^2(\phi) \quad (88)$$

$$p'_{12} = p_{13} \sin^4(\phi) - p_{44} \sin^2(2\phi) + p_{31} \cos^4(\phi) + p_{11} \sin^2(\phi) \cos^2(\phi) + p_{33} \sin^2(\phi) \cos^2(\phi) \quad (89)$$

$$p'_{13} = p_{12} \sin^2(\phi) + p_{31} \cos^2(\phi) \quad (90)$$

$$p'_{14} = p_{14} \sin^3(\phi) - 2p_{41} \sin(\phi) \cos^2(\phi) \quad (91)$$

$$p'_{15} = (p_{14} + 2p_{41}) \sin^2(\phi) \cos(\phi) \quad (92)$$

$$p'_{16} = \sin(\phi) \cos(\phi) \left(-p_{11} \sin^2(\phi) + p_{13} \sin^2(\phi) - p_{31} \cos^2(\phi) + p_{33} \cos^2(\phi) - 2p_{44} \cos(2\phi) \right) \quad (93)$$

$$p'_{21} = p_{31} \sin^4(\phi) - p_{44} \sin^2(2\phi) + p_{13} \cos^4(\phi) + p_{11} \sin^2(\phi) \cos^2(\phi) + p_{33} \sin^2(\phi) \cos^2(\phi) \quad (94)$$

$$p'_{22} = p_{11} \cos^4(\phi) + \sin^2(\phi) \left(p_{33} \sin^2(\phi) + p_{13} \cos^2(\phi) + p_{31} \cos^2(\phi) + 4p_{44} \cos^2(\phi) \right) \quad (95)$$

$$p'_{23} = p_{31} \sin^2(\phi) + p_{12} \cos^2(\phi) \quad (96)$$

$$p'_{24} = (p_{14} + 2p_{41}) \sin(\phi) \cos^2(\phi) \quad (97)$$

$$p'_{25} = p_{14} \cos^3(\phi) - 2p_{41} \sin^2(\phi) \cos(\phi) \quad (98)$$

$$p'_{26} = \sin(\phi) \cos(\phi) \left(-p_{31} \sin^2(\phi) + p_{33} \sin^2(\phi) - p_{11} \cos^2(\phi) + p_{13} \cos^2(\phi) + 2p_{44} \cos(2\phi) \right) \quad (99)$$

$$p'_{31} = p_{12} \sin^2(\phi) + p_{13} \cos^2(\phi) \quad (100)$$

$$p'_{32} = p_{13} \sin^2(\phi) + p_{12} \cos^2(\phi) \quad (101)$$

$$p'_{33} = p_{11} \quad (102)$$

$$p'_{34} = p_{14}(-\sin(\phi)) \quad (103)$$

$$p'_{35} = p_{14}(-\cos(\phi)) \quad (104)$$

$$p'_{36} = (p_{13} - p_{12}) \sin(\phi) \cos(\phi) \quad (105)$$

$$p'_{41} = p_{41} \sin^3(\phi) - 2p_{14} \sin(\phi) \cos^2(\phi) \quad (106)$$

$$p'_{42} = (2p_{14} + p_{41}) \sin(\phi) \cos^2(\phi) \quad (107)$$

$$p'_{43} = p_{41}(-\sin(\phi)) \quad (108)$$

$$p'_{44} = p_{44} \sin^2(\phi) + \frac{1}{2} (p_{11} - p_{12}) \cos^2(\phi) \quad (109)$$

$$p'_{45} = \frac{1}{2} (-p_{11} + p_{12} + 2p_{44}) \sin(\phi) \cos(\phi) \quad (110)$$

$$p'_{46} = \cos(\phi) \left(p_{14} \cos(2\phi) - p_{41} \sin^2(\phi) \right) \quad (111)$$

$$p'_{51} = (2p_{14} + p_{41}) \sin^2(\phi) \cos(\phi) \quad (112)$$

$$p'_{52} = p_{41} \cos^3(\phi) - 2p_{14} \sin^2(\phi) \cos(\phi) \quad (113)$$

$$p'_{53} = p_{41} (-\cos(\phi)) \quad (114)$$

$$p'_{54} = \frac{1}{2} (-p_{11} + p_{12} + 2p_{44}) \sin(\phi) \cos(\phi) \quad (115)$$

$$p'_{55} = \frac{1}{2} (p_{11} - p_{12}) \sin^2(\phi) + p_{44} \cos^2(\phi) \quad (116)$$

$$p'_{56} = -\sin(\phi) (p_{41} \cos^2(\phi) + p_{14} \cos(2\phi)) \quad (117)$$

$$p'_{61} = \sin(\phi) \cos(\phi) (-p_{11} \sin^2(\phi) + p_{31} \sin^2(\phi) + 2p_{44} \sin^2(\phi) - p_{13} \cos^2(\phi) + (p_{33} - 2p_{44}) \cos^2(\phi)) \quad (118)$$

$$p'_{62} = \cos(\phi) (p_{33} \sin^3(\phi) + p_{31} \sin(\phi) \cos^2(\phi) + p_{44} \sin(2\phi) \cos(\phi)) \\ - \sin(\phi) (p_{11} \cos^3(\phi) + (p_{13} + 2p_{44}) \sin^2(\phi) \cos(\phi)) \quad (119)$$

$$p'_{63} = (p_{31} - p_{12}) \sin(\phi) \cos(\phi) \quad (120)$$

$$p'_{64} = \cos(\phi) (p_{41} \cos(2\phi) - p_{14} \sin^2(\phi)) \quad (121)$$

$$p'_{65} = -\sin(\phi) (p_{14} \cos^2(\phi) + p_{41} \cos(2\phi)) \quad (122)$$

$$p'_{66} = \cos^2(\phi) ((p_{33} - p_{31}) \sin^2(\phi) + p_{44} \cos(2\phi)) - \sin^2(\phi) ((p_{13} - p_{11}) \cos^2(\phi) + p_{44} \cos(2\phi)) \quad (123)$$